Figure 3. $Nfkbiz^{-/-}$ Mice Develop SS-like Autoimmune Disease

(A) Immunostaining of periocular skin of wild-type mice with serum from $Nfkbiz^{+/+}$ (+/+) or $Nfkbiz^{-/-}$ (−/−) mice. Sections of periocular skin were incubated with mouse serum and then stained with Alexa Fluor 488-conjugated anti-mouse IgG (green). The nuclei were stained with DAPI (red).

(B) Serum concentrations of anti-nuclear antibody (ANA) in $Nfkbiz^{+/+}$ and $Nfkbiz^{-/-}$ mice.

(C) Histology of the lacrimal glands of 5-month-old $Nfkbiz^{-/-}$ and $Nfkbiz^{+/+}$ littermate mice. Sections of the lacrimal glands were stained with HE or immunostained with either CD3 (green) and B220 (red) antibodies or CD4 (red) and CD8 (green) antibodies. The nuclei were stained with DAPI (blue).

(D) Tear secretion volume in 2-month-old $Nfkbiz^{+/+}$ (+/+), $Nfkbiz^{+/-}$ (+/−), and $Nfkbiz^{-/-}$ (−/−) littermate mice. Tear volume was measured by a modified Schirmer test. Data shown are mean ± SEM (n = 5).

(E and F) Serum concentrations of SSA and SSB antibodies in $Nfkbiz^{+/+}$ and $Nfkbiz^{-/-}$ mice.

(G) Pneumonia in $Nfkbiz^{-/-}$ mice. Paraffin sections from a pneumonic lung of a $Nfkbiz^{-/-}$ (−/−) mouse and the lung of a littermate control $Nfkbiz^{+/+}$ (+/+) mouse were stained with HE.

Antibody concentrations in serum were measured by ELISA. Horizontal bars show the mean value. $*p < 0.05$, $**p < 0.01$, and $***p < 0.001$. See also Table S1.

mice (Clausen et al., 1999) to evaluate the possible roles of myeloid cells. In LysM-Cre;$Nfkbiz^{flox/flox}$ mice, lipopolysaccharide-induced IκB-ζ expression in bone marrow-derived macrophages from LysM-Cre;$Nfkbiz^{flox/flox}$ mice was severely suppressed, indicating the efficient disruption of the $Nfkbiz$ locus in myeloid cells (Figure S4J). However, the mutant mice did not exhibit inflammation (Figure S4G), indicating that IκB-ζ deficiency in myeloid cells is not the major cause of disease. These results are consistent with the conclusion that IκB-ζ deficiency in hematopoietic cells is not a cause of the disease.

IκB-ζ Deficiency in Epithelial Cells Causes SS-like Inflammation

The above experiments suggested a critical role for nonhematopoietic cells in inducing inflammation in IκB-ζ-deficient mice. Because the inflammation is localized to the lacrimal glands, conjunctiva, and facial skin, we suspected that dysfunction of epithelial cells might be involved in the pathogenesis. We thus bred the $Nfkbiz$-floxed mice with K5-Cre mice (Tarutani et al., 1997), in which the Cre recombinase is expressed under the promoter of keratin 5 ($Krt5$), a marker of epithelial cells. Immunohistochemical analysis revealed the specific expression of keratin 5 in the epidermis and epithelial cells in the conjunctiva and
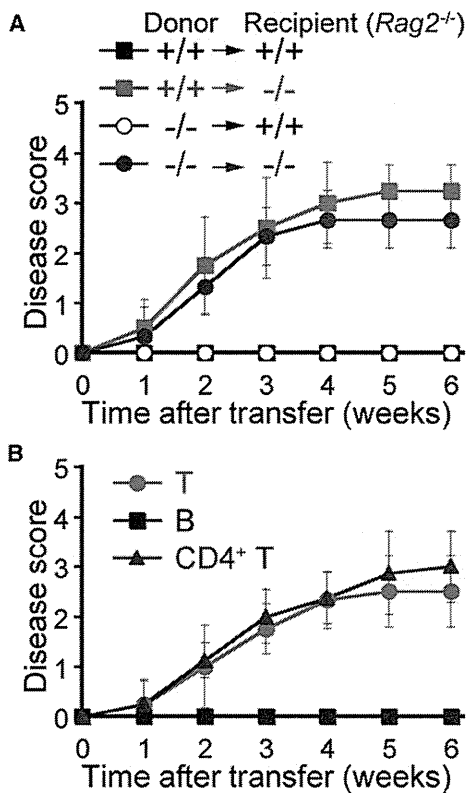
$Nfkbiz^{flox/flox}$ mice were then bred with various Cre-expressing mice to establish cell type-specific mutant mice. Neither Lck-Cre;$Nfkbiz^{\Delta/flox}$ nor Mb1-Cre;$Nfkbiz^{flox/flox}$ mice, which specifically lacked IκB-ζ in T or B cells (Hobeika et al., 2006; Takahama et al., 1998), exhibited any apparent inflammation up to 30 weeks after birth (Figures S4G–S4I). These observations were consistent with the results obtained from adoptive transfer analysis, further ruling out the pathological role of IκB-ζ deficiency in lymphocytes. We also bred $Nfkbiz^{flox/flox}$ mice and LysM-Cre

Figure 4. IκB-ζ Deficiency in Lymphocytes Is Not Essential for Inflammation in Nfkbiz⁻/⁻ Mice

(A) Progression of inflammation in mice after adoptive transfer. Splenocytes (1 × 10⁷ cells) from $Nfkbiz^{+/+}$ or $Nfkbiz^{-/-}$ mice were adoptively transferred to $Nfkbiz^{+/+}Rag2^{-/-}$ or $Nfkbiz^{-/-}Rag2^{-/-}$ mice. +/+ and −/− indicate the genotypes of the *Nfkbiz* alleles. Pathological phenotypes were scored as in Figure S1 after adoptive transfer (n = 3–4).

(B) Progression of inflammation in $Nfkbiz^{-/-}Rag2^{-/-}$ mice transplanted with T, B, or CD4⁺ T cells. Purified T cells (3 × 10⁶ cells), B cells (3 × 10⁶ cells), or CD4⁺ T cells (2 × 10⁶ cells) from $Nfkbiz^{+/+}$ mice were transplanted into $Nfkbiz^{-/-}Rag2^{-/-}$ mice (n = 4–8).

The disease scores are shown as mean ± SD. See also Figure S3.

the lacrimal glands, including both ductules and acini, in addition to epithelial cells in the medullary thymus (Figure 5A). As expected from the epithelial-specific disruption, marked reduction of *Nfkbiz* mRNA expression was observed in the skin, conjunctiva, and lacrimal glands, but not in the lymph nodes, of K5-Cre;$Nfkbiz^{flox/flox}$ mice, whereas the expression was normal in stimulated T and B cells and macrophages (Figures 5B and S4H–S4J). K5-Cre;$Nfkbiz^{flox/flox}$ mice lacking IκB-ζ in epithelial cells exhibited inflammation similar to $Nfkbiz^{-/-}$ mice (Figures 5C–5G and S4K). In spite of delayed onset and milder progression of the symptoms, inflammation with infiltrating lymphocytes was observed in the periocular skin, conjunctiva, and lacrimal glands of the K5-Cre;$Nfkbiz^{flox/flox}$ mice. Moreover, a significant elevation of both SSA and SSB antibodies was detected. These results indicate that IκB-ζ deficiency in the epithelial tissues is sufficient to induce the SS-like autoimmune disease.

Enhanced Apoptosis in IκB-ζ-Deficient Lacrimal Glands Is Associated with SS-like Inflammation

It has been reported that aberrant apoptosis was observed in the exocrine glands of SS patients (Manganelli and Fietta, 2003; Matsumura et al., 1998; Nakamura et al., 1998; Polihronis et al., 1998) and animal models of the disease (Ishimaru et al., 1999; Saegusa et al., 2002). We therefore examined apoptosis in the lacrimal glands. Compared with control mice, increased TUNEL-positive cells were detected in the lacrimal glands of $Nfkbiz^{-/-}$ and K5-Cre;$Nfkbiz^{flox/flox}$ mice (Figures 6A and S5A). It is noteworthy that the lacrimal glands of $Nfkbiz^{-/-}Rag2^{-/-}$ mice, in which inflammation was not apparent, also exhibited excessive apoptotic cells, indicating that the enhanced apoptosis did not result from inflammation. Consistent with the increased apoptosis, caspase 3 processing in the lacrimal glands was upregulated in $Nfkbiz^{-/-}$ mice regardless of the occurrence of inflammation (Figure 6B).

The enhanced apoptosis in IκB-ζ-deficient lacrimal glands prompted us to examine the role of IκB-ζ in regulation of apoptosis. The mouse keratinocyte cell line Pam212 was infected with retrovirus harboring IκB-ζ cDNA and effects of IκB-ζ expression on apoptosis was examined. Among three alternative splicing variants of IκB-ζ (Motoyama et al., 2005; Yamazaki et al., 2005), cells expressing IκB-ζ(L) and IκB-ζ(S), but not IκB-ζ(D), exhibited markedly reduced early apoptosis and secondary necrosis induced by tunicamycin or etoposide (Figures 6C, S5B, and S5C).

To determine whether the increased apoptosis caused the SS-like inflammation, we intravenously administered the pan-caspase inhibitor Z-VAD-FMK or the caspase-3, caspase-7, caspase-8-directed inhibitor Ac-DEVD-CHO into the right eye of $Nfkbiz^{-/-}$ mice from 4 to 7 weeks after birth, a period when most of the mutant mice developed the autoimmune disorder. Administration of the caspase inhibitors suppressed apoptosis in the lacrimal glands of $Nfkbiz^{-/-}$ mice (Figure 6D). Compared with mice treated with vehicle or a negative control, Z-FA-FMK, dramatic amelioration of inflammatory lesions was observed at 8 weeks in the eye treated with either caspase inhibitor but not in the other eye (Figures 6E, 6F, and S5D). Accordingly, tear secretion was increased in the inhibitor-administered eyes (Figure 6G). These findings strongly suggest that enhanced apoptosis in the IκB-ζ-deficient epithelial cells is the primary cause of the SS-like autoimmune disease in IκB-ζ-deficient mice.

Expression of IκB-ζ in the Lacrimal Glands Requires STAT3

Previous reports showed that IκB-ζ expression requires MyD88-dependent or STAT3-dependent signals (Okamoto et al., 2010; Yamamoto et al., 2004). Because MyD88-deficient mice do not exhibit apparent inflammation, we suspected that STAT3 might be involved in the expression of IκB-ζ in epithelial cells. Because STAT3-deficient mice are embryonic lethal (Takeda et al., 1997), we created epithelial cell-specific STAT3-deficient mice (K5-Cre;$Stat3^{flox/flox}$) and examined IκB-ζ expression in the lacrimal glands. A previous report showed that although migration of keratinocytes during wound healing was impaired, keratinocyte proliferation and the development of the epidermis were normal in the epithelial STAT3 knockout mice (Sano et al., 1999).
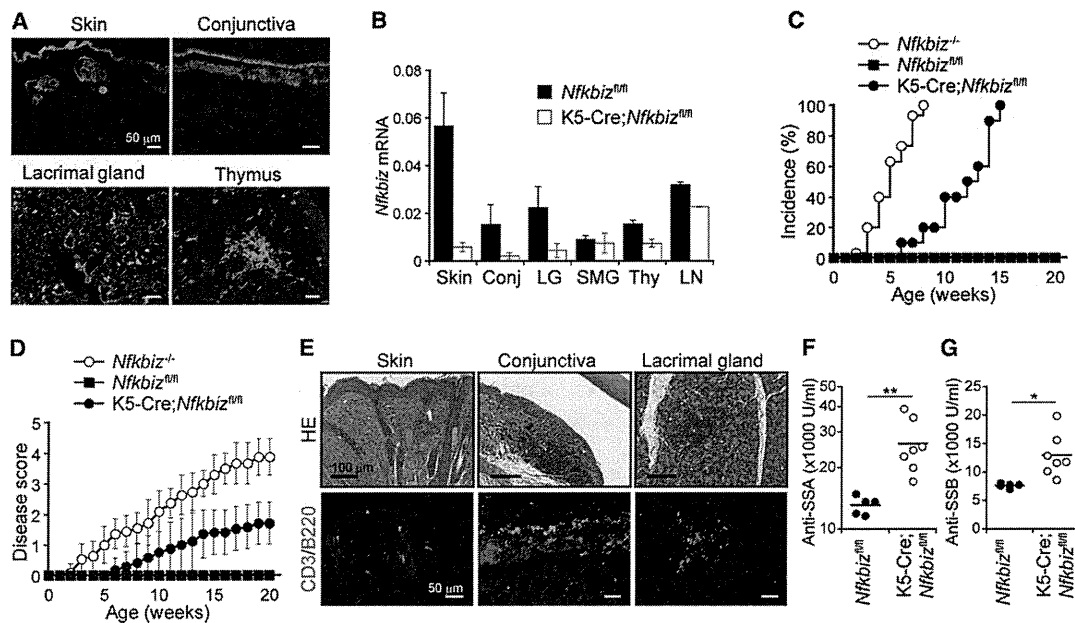
Figure 5. IκB-ζ Deficiency in Epithelial Cells Causes Inflammation

(A) Expression of keratin 5 in the skin, conjunctiva, lacrimal glands, and thymus. Sections of the indicated tissues from wild-type mice were stained with keratin 5 antibodies (green). The nuclei were stained with DAPI (blue).

(B) Expression of *Nfkbiz* mRNA in tissues of *Nfkbiz*$^{flox/flox}$ and K5-Cre;*Nfkbiz*$^{flox/flox}$ mice. *Nfkbiz* mRNA was quantitated by real-time RT-PCR in the indicated *Krt5*-expressing tissues from *Nfkbiz*$^{flox/flox}$ and K5-Cre;*Nfkbiz*$^{flox/flox}$ mice. Abbreviations are as follows: Conj, conjunctiva; LG, lacrimal gland; SMG, submandibular gland; Thy, thymus; LN, lymph node. Data shown are mean ± SEM (n = 3).

(C and D) Incidence (C) and progression of inflammation (D) in K5-Cre;*Nfkbiz*$^{flox/flox}$ mice. Pathological phenotypes of *Nfkbiz*$^{-/-}$ (n = 30), *Nfkbiz*$^{flox/flox}$ (n = 10), and K5-Cre;*Nfkbiz*$^{flox/flox}$ (n = 10) mice were scored as in Figure S1 after birth. The disease scores are shown as mean ± SD.

(E) Histology of the periocular skin, conjunctiva, and lacrimal glands in 5-month-old K5-Cre;*Nfkbiz*$^{flox/flox}$ mice. Sections of the indicated tissues were stained with HE or immunostained with CD3 (green) and B220 (red) antibodies. The nuclei were stained with DAPI (blue).

(F and G) Serum concentrations of SSA (F) and SSB (G) antibodies in *Nfkbiz*$^{flox/flox}$ and K5-Cre;*Nfkbiz*$^{flox/flox}$ mice. Antibody concentrations in serum were measured by ELISA. Horizontal bars show the mean value. *p < 0.05 and **p < 0.01.

See also Figure S4.

Whereas IκB-ζ expression in the lacrimal glands was clearly detected in wild-type mice, the expression of IκB-ζ was significantly reduced in K5-Cre;*Stat3*$^{flox/flox}$ mice, indicating a critical role for STAT3 in the expression of IκB-ζ (Figure 7A).

Moreover, K5-Cre;*Stat3*$^{flox/flox}$ mice developed periocular inflammation similar to K5-Cre;*Nfkbiz*$^{flox/flox}$ mice, both in the timing of onset and the severity of the symptoms (Figures 7B, 7C, and S7). In addition to lymphocyte-infiltrating periocular dermatitis, conjunctivitis, and dacryoadenitis, elevated SSA and SSB antibody titers were detected in K5-Cre;*Stat3*$^{flox/flox}$ mice (Figures 7D–7F). Collectively, these data strongly suggest that STAT3-dependent IκB-ζ expression plays a critical homeostatic role in epithelial tissues such as the lacrimal glands and that defects in this homeostasis lead to the SS-like autoimmune disease.

DISCUSSION

In the present study, we have shown that the spontaneous development of inflammation in IκB-ζ-deficient mice is accompanied by histological and functional abnormalities in the lacrimal glands and the production of anti-nuclear antibodies, including SSA and SSB antibodies. These characteristics fulfill the diag-

nostic criteria for SS in humans (Vitali et al., 2002), and hence IκB-ζ-deficient mice provide a unique animal model for the disease based on mutation of a single gene. Most of the previous studies on SS model mice showed that abnormalities in lymphocytes induced the autoimmune exocrinopathy (Groom et al., 2002; Li et al., 2004; Peng et al., 2010). In contrast, this study has demonstrated that abnormalities in epithelial tissues are also sufficient to elicit SS-like autoimmune disease. We observed no obvious symptoms in the salivary glands in IκB-ζ-deficient mice, in common with some SS patients (Al-Hashimi et al., 2001; Vissink et al., 2003), suggesting the presence of IκB-ζ-independent homeostatic mechanisms in the salivary epithelium. Intriguingly, the salivary glands of K5-Cre;*Nfkbiz*$^{-/-}$ mice exhibited sustained expression of IκB-ζ.

Although previous studies demonstrated critical roles of IκB-ζ in the responses of macrophages to pathogens (Motoyama et al., 2005; Yamamoto et al., 2004) and in Th17 cell development (Okamoto et al., 2010), this study showed that defects in hematopoietic cells, including macrophages, dendritic cells, and T cells, are not essential for inflammation in IκB-ζ-deficient mice. Although SSA and SSB antibodies are often detected in SS patients, our transfer experiments showed that only CD4$^+$ T cells are required to elicit the disease in *Nfkbiz*$^{-/-}$*Rag2*$^{-/-}$
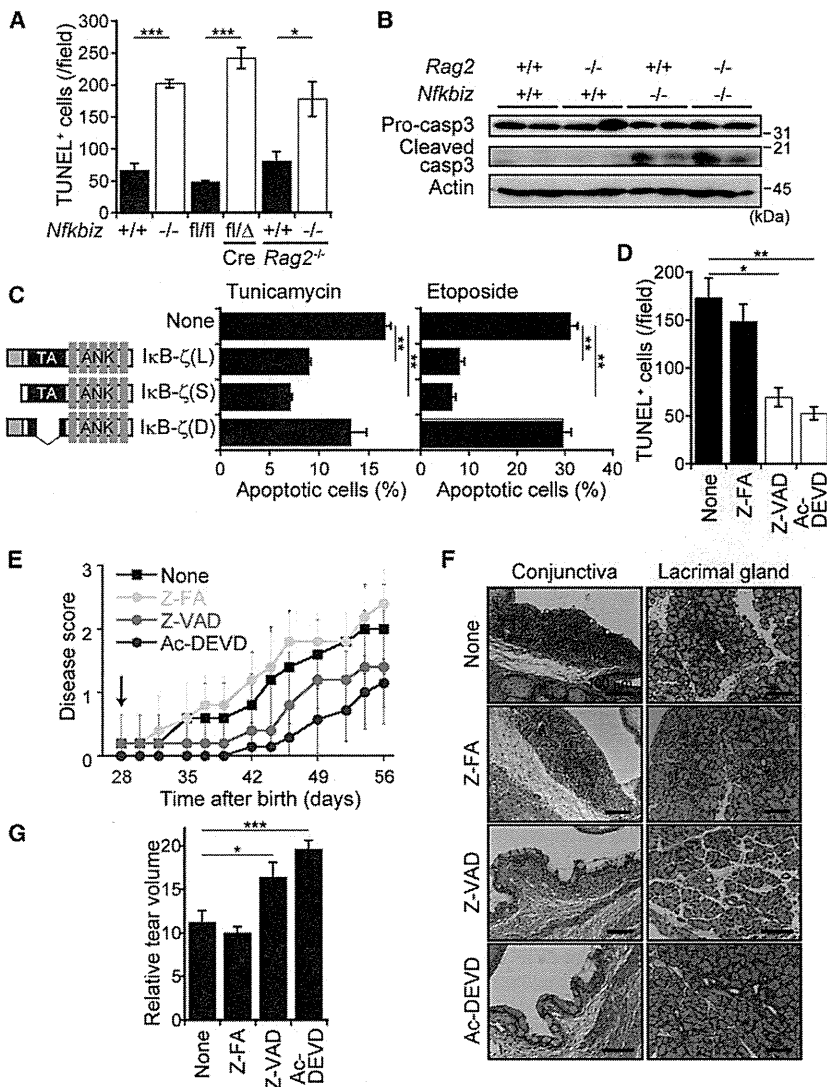
Figure 6. Enhanced Apoptosis in the IκB-ζ-Deficient Lacrimal Glands Is Associated with SS-like Inflammation

(A) Apoptosis in the lacrimal glands of the mice. TUNEL assays were performed with sections from the lacrimal glands of $Nfkbiz^{+/+}$, $Nfkbiz^{-/-}$, $Nfkbiz^{flox/flox}$, K5-Cre;$Nfkbiz^{flox/flox}$, $Rag2^{-/-}$, and $Nfkbiz^{-/-}Rag2^{-/-}$ mice. The numbers of TUNEL-positive cells were quantitated (n = 3).

(B) Caspase processing in the lacrimal glands of the mice. Lysates prepared from the lacrimal glands of $Nfkbiz^{+/+}$, $Nfkbiz^{-/-}$, $Rag2^{-/-}$, and $Nfkbiz^{-/-}Rag2^{-/-}$ mice were immunoblotted with caspase-3 and β-actin antibodies.

(C) Antiapoptotic activity of IκB-ζ. Pam212 cells were retrovirally transduced to express IκB-ζ(L), IκB-ζ(S), or IκB-ζ(D) and the green fluorescence protein (GFP). Apoptosis was induced with 100 ng/ml of tunicamycin or 100 μM of etoposide for 24 hr and cells were subjected to flow cytometric analysis after annexin V and DAPI staining. Percent frequencies of early apoptotic cells (annexin V-positive and DAPI-negative) in GFP-positive cells are shown (n = 2). Data shown are representative of three independent experiments. Abbreviations are as follows: TA, transactivation domain; ANK, ankyrin repeats.

(D–G) Phenotypes of $Nfkbiz^{-/-}$ mice administered with caspase inhibitors. 100 nmol/mouse of Z-FA-FMK (n = 5), Z-VAD-FMK (n = 5), Ac-DEVD-CHO (n = 7), or vehicle (None; n = 5) were injected three times per week into the fundus vein in the right eye of 4-week-old $Nfkbiz^{-/-}$ mice. The numbers of TUNEL-positive cells in the lacrimal glands were quantitated (n = 3) (D). Progression of the inflammation (E) and histology of the conjunctiva and lacrimal glands (F) on the right side of the face and tear secretion volume from the right eyes (G) of $Nfkbiz^{-/-}$ mice after administration of the inhibitors for 4 weeks are shown. The arrow in (E) indicates the day administration was started. The disease scores are shown as mean ± SD.

Data are shown as mean ± SEM. *p < 0.05, **p < 0.01, and ***p < 0.001. See also Figure S5.

mice, indicating that B cells are dispensable for the inflammation. Thus, the autoantibodies are generated by the inflammation but are not a direct cause of the disease in IκB-ζ-deficient mice. Instead, dysfunction of epithelial cells lacking IκB-ζ is critically involved in the development of the disease.

We found in this study that epithelial deletion of STAT3 also induced the SS-like symptoms. Because IκB-ζ expression was significantly reduced in the lacrimal glands of STAT3-deficient mice, STAT3 is required for the expression of IκB-ζ. Although the identity of an inducer(s) that elicits IκB-ζ expression is currently unknown, our preliminary study revealed that EGF or epiregulin elicited STAT3 phosphorylation and IκB-ζ induction in keratinocytes. Because EGF is constitutively secreted in tears by the lacrimal glands (Dartt, 2004) and its concentration is decreased in SS patients (Pflugfelder et al., 1999), EGF or its homologs may elicit IκB-ζ expression via STAT3 activation in epithelial tissues such as the lacrimal glands. Although in situ hybridization detected *Nfkbiz* mRNA in various organs in lipopolysaccharide-treated mice, it failed to detect IκB-ζ expression

in any tissues in untreated mice, including the lacrimal glands (data not shown), indicating that the expression of IκB-ζ is kept at low levels in healthy animals. Thus, homeostatic expression of IκB-ζ is quantitatively different from IκB-ζ induction upon infection with pathogens. We propose here that the constitutive induction of IκB-ζ is critical for homeostasis in tissues such as the lacrimal glands.

Epithelial deletion of IκB-ζ resulted in the acceleration of apoptosis in the lacrimal glands. Accumulating evidence suggests that aberrant apoptosis plays a key role in the pathogenesis of various autoimmune diseases, including SS (Apostolou et al., 2003; Giordano et al., 1997; Ito et al., 1997; Matsumura et al., 1998; Nakamura et al., 1998). Enhanced apoptosis is considered to be involved in the impairment of secretory function and the generation of cryptic epitopes of autoantigens such as α-fodrin (Haneji et al., 1997; Huang et al., 2005; Nagaraju et al., 2001; Saegusa et al., 2002). Amelioration of the symptoms by local administration of caspase inhibitors supports the critical role of apoptosis in the development of inflammation. It is to be
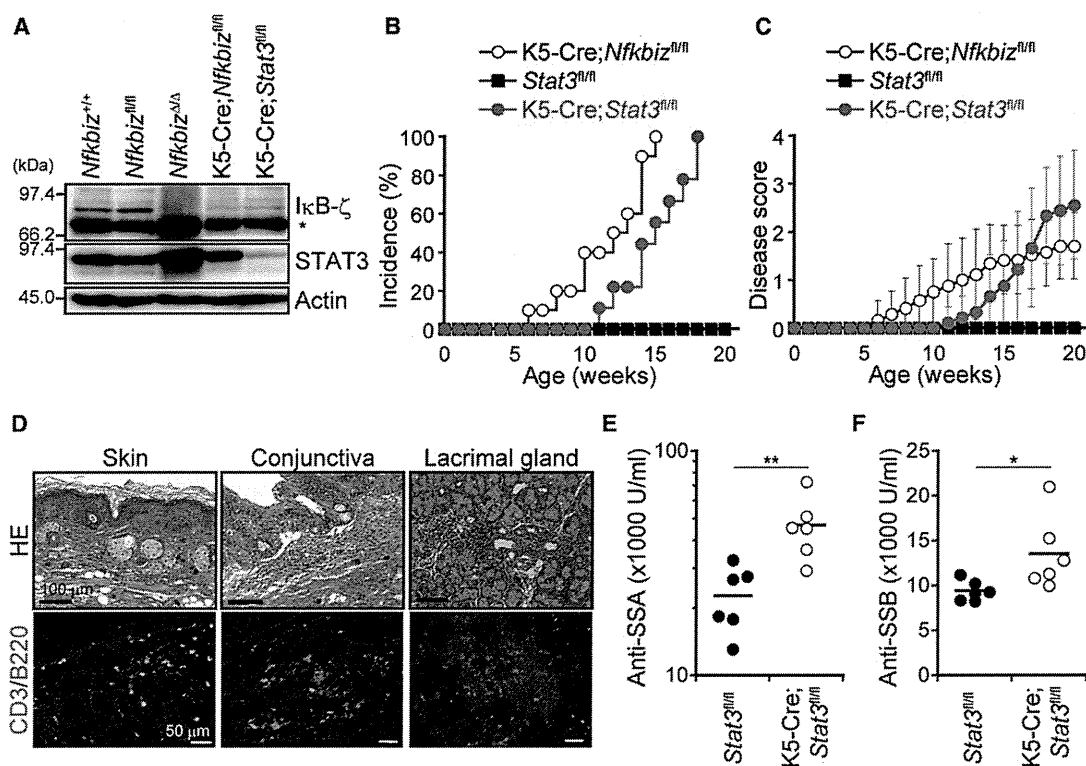
Figure 7. K5-Cre;Stat3$^{flox/flox}$ Mice Develop SS-like Inflammation

(A) Expression of IκB-ζ in the lacrimal glands. Lysates prepared from the lacrimal glands of Nfkbiz$^{+/+}$, Nfkbiz$^{flox/flox}$, Nfkbiz$^{\Delta/\Delta}$, K5-Cre;Nfkbiz$^{flox/flox}$, and K5-Cre;Stat3$^{flox/flox}$ mice were immunoblotted with IκB-ζ, STAT3, and β-actin antibodies. An asterisk indicates a nonspecific band.

(B and C) Incidence (B) and progression (C) of inflammation in K5-Cre;Nfkbiz$^{flox/flox}$, Stat3$^{flox/flox}$, and K5-Cre;Stat3$^{flox/flox}$ mice. The disease scores are shown as mean ± SD (n = 10).

(D) Histology of the periocular skin, conjunctiva, and lacrimal glands of 5-month-old K5-Cre;Stat3$^{flox/flox}$ mice. Sections of the indicated tissues were stained with HE or immunostained with CD3 (green) and B220 (red) antibodies. The nuclei were stained with DAPI (blue).

(E and F) Serum concentrations of SSA (E) and SSB (F) antibodies in Stat3$^{flox/flox}$ and K5-Cre;Stat3$^{flox/flox}$ mice. Horizontal bars show the mean value. *p < 0.05 and **p < 0.01.

See also Figure S6.

noted that increased apoptosis was also observed in Nfkbiz$^{-/-}$ Rag2$^{-/-}$ mice that lack infiltrating lymphocytes. Thus, the acceleration of apoptosis is not caused by inflamed leukocytes, but precedes the inflammation that requires T cells, in sharp contrast to T cell-mediated apoptosis (Kong et al., 1997; Polihronis et al., 1998; Wu et al., 1996). Because some Nfkbiz$^{-/-}$Rag2$^{-/-}$ mice exhibited weak inflammation with delayed onset, it is likely that continuously enhanced apoptosis in the IκB-ζ-deficient epithelial cells eventually induces inflammation, possibly dependent on myeloid cells in the absence of infiltrating lymphocytes. Considering that apoptosis is enhanced in IκB-ζ-deficient lacrimal glands, the simplest explanation is that IκB-ζ plays a protective role against apoptosis, which is evoked possibly by persistent endoplasmic reticulum stress in tissues such as the lacrimal glands that secrete a large amount of protein (Hetz, 2012). In fact, expression of IκB-ζ(L) or IκB-ζ(S) in Pam212 cells conferred resistance to apoptosis induced by endoplasmic reticulum stress with tunicamycin. The observation that IκB-ζ(D) lacking the transactivation domain (Motoyama et al., 2005) failed to exhibit the activity strongly suggests that IκB-ζ-mediated gene activation is required for the antiapoptotic activity. Furthermore,

it has been reported that EGF, which is capable of inducing IκB-ζ expression in a STAT3-dependent manner, significantly suppresses apoptosis in conjunctival epithelial cells both in vitro and in vivo (Higuchi et al., 2006; Xiao et al., 2012).

This study uncovered a pathogenic mechanism of SS-like inflammation in which apoptosis in epithelial cells enhanced by deletion of IκB-ζ or STAT3 elicits the autoimmune activation of lymphocytes, which culminates in the development of inflammation. This mechanism may underlie SS pathogenesis in some patients. Further studies on the molecular basis of the homeostatic mechanisms in tissues will provide new diagnostic and/ or therapeutic strategies for SS and other tissue-specific autoimmune diseases.

EXPERIMENTAL PROCEDURES

Mice

C57BL/6 mice were purchased from Charles River Laboratories Japan (Yokohama, Japan). Nfkbiz$^{-/-}$ mice were described previously (Yamamoto et al., 2004). Age- and sex-matched littermates were used as controls. Rag2$^{-/-}$ mice on a C57BL/6 background were obtained from the Central Institute for Experimental Animals (Kawasaki, Japan). B6-Tg(CAG-FLPe)36 mice (Kanki

et al., 2006) (RBRC01834) were provided by RIKEN BioResource Center through the National Bio-Resource Project of the MEXT, Japan. $Tnf^{-/-}$ mice (Taniguchi et al., 1997) and $Stat3^{flox/flox}$ mice (Takeda et al., 1998); CAG-Cre (Sakai and Miyazaki, 1997), Lck-Cre (Takahama et al., 1998), LysM-Cre (Clausen et al., 1999), and K5-Cre (Tarutani et al., 1997) transgenic mice; and Mb1-Cre knockin mice (Hobeika et al., 2006) were described previously. All mice were maintained under specific-pathogen-free conditions in the animal facilities of Tohoku University. Animal experiment protocols were approved by the Institutional Animal Care and Use Committee.

$Nfkbiz^{flox/flox}$ Mice

A targeting vector for the $Nfkbiz^{flox/flox}$ mice was constructed to delete exons 5, 6, and 7 of the $Nfkbiz$ gene. Genomic fragments of $Nfkbiz$ were generated by PCR and cloned with loxP sequences and a Neo cassette flanked by FRT sequences into a pBluescript plasmid harboring a loxP-Neo cassette, as shown in Figure S4. The targeting construct was linearized and introduced by electroporation into the Bruce4 embryonic stem cells derived from C57BL/6. Clones doubly resistant to G418 and ganciclovir were screened for homologous recombination by PCR and Southern blotting. The sequences of the PCR primers used for genotyping are shown in Supplemental Experimental Procedures. The obtained embryonic stem cell clones bearing the correctly targeted locus were injected into BALB/c blastocysts and chimeric male offspring were obtained. The chimeric mice were mated with C57BL/6 mice to establish a strain with a germline-transmitted locus. The resulting mice were bred with B6-Tg(CAG-FLPe)36 mice (Kanki et al., 2006) to delete the Neo cassette.

Disease Score

Pathological phenotypes of mice were scored according to the following criteria: 1, periorbital swelling; 2, eyes with discharge that were difficult to open; 3, periocular skin erosion; 4, inflammation reaching perioral skin; 5, erosion and loss of hair in whole face.

Tear Secretion Test

Eight-week-old $Nfkbiz^{-/-}$ or wild-type mice anesthetized with pentobarbital were intraperitoneally injected with 5 μg/g body weight of pilocarpine hydrochloride to stimulate tear production. Tears were measured by a modified Schirmer test via Zone-Quick (Showa Yakuhin Kako, Tokyo, Japan) at 5 min after pilocarpine injection.

Quantitative PCR

Total RNA isolated with RNAiso plus (Takara Bio, Otsu, Japan) was reverse transcribed with Multiscribe Reverse Transcriptase (Life Technologies, Carlsbad, CA). The cDNA was analyzed by quantitative real-time PCR with SYBR Premix Ex Taq II (Takara Bio) on the LightCycler system 330 (Roche). The sequences of the primers used are shown in Supplemental Experimental Procedures.

Adoptive Transfer

Whole splenocytes or lymph node cells were prepared from wild-type or $Nfkbiz^{-/-}$ mice. Red blood cells in splenocytes were lysed in 144 mM NH_4Cl, 17 mM Tris-HCl (pH 7.7). 1×10^7 cells per mouse were injected intravenously into 6- to 10-week-old $Rag2^{-/-}$ or $Nfkbiz^{-/-}Rag2^{-/-}$ mice.

Retroviral Transduction

FLAG-tagged IκB-ζ cDNA was cloned into pMY-IRES-EGFP (Kitamura et al., 2003). Recombinant retroviruses were prepared by transfecting the Plat-E packaging cells with the plasmid by FuGENE6 (Roche Diagnostics, Indianapolis, IN) as previously described (Morita et al., 2000). Pam212 cells were infected with the retrovirus in the presence of 2 μg/ml polybrene (Merck Millipore) for 24 hr.

In Vitro Apoptosis Assay

Retrovirally transduced Pam212 cells were treated 100 ng/ml of tunicamycin or 100 μM of etoposide for 24 hr. Apoptotic cell staining was performed with Annexin V Apoptosis Detection Kit APC (eBioscience, San Diego, CA), according to the manufacturer's instructions except that 4',6-diamidino-2-phenylindole (DAPI) was used instead of propidium iodide.

In Vivo Caspase Inhibitor Administration

100 nmol of Z-FA-FMK, Z-VAD-FMK, Ac-DEVD-CHO, or 10% dimethyl sulfoxide in PBS as a vehicle control were injected into the fundus vein in the right eyes of 4-week-old $Nfkbiz^{-/-}$ mice three times per week for 4 weeks. Tear secretion and histopathology were examined when the mice were 8 weeks old.

Statistical Analysis

Paired data were evaluated with Student's t test. A value of $p < 0.05$ was considered statistically significant.

SUPPLEMENTAL INFORMATION

Supplemental Information includes Supplemental Experimental Procedures, six figures, and one table and can be found with this article online at http://dx.doi.org/10.1016/j.immuni.2012.11.016.

REFERENCES

Al-Hashimi, I., Khuder, S., Haghighat, N., and Zipp, M. (2001). Frequency and predictive value of the clinical manifestations in Sjögren's syndrome. J. Oral Pathol. Med. 30, 1–6.

Apostolou, I., Hao, Z., Rajewsky, K., and von Boehmer, H. (2003). Effective destruction of Fas-deficient insulin-producing beta cells in type 1 diabetes. J. Exp. Med. 198, 1103–1106.

Clausen, B.E., Burkhardt, C., Reith, W., Renkawitz, R., and Förster, I. (1999). Conditional gene targeting in macrophages and granulocytes using LysMcre mice. Transgenic Res. 8, 265–277.

Dartt, D.A. (2004). Interaction of EGF family growth factors and neurotransmitters in regulating lacrimal gland secretion. Exp. Eye Res. 78, 337–345.

Eto, A., Muta, T., Yamazaki, S., and Takeshige, K. (2003). Essential roles for NF-κ B and a Toll/IL-1 receptor domain-specific signal(s) in the induction of I κ B-ζ. Biochem. Biophys. Res. Commun. 301, 495–501.

Fox, R.I. (2005). Sjögren's syndrome. Lancet 366, 321–331.

Giordano, C., Stassi, G., De Maria, R., Todaro, M., Richiusa, P., Papoff, G., Ruberti, G., Bagnasco, M., Testi, R., and Galluzzo, A. (1997). Potential involvement of Fas and its ligand in the pathogenesis of Hashimoto's thyroiditis. Science 275, 960–963.

Groom, J., Kalled, S.L., Cutler, A.H., Olson, C., Woodcock, S.A., Schneider, P., Tschopp, J., Cachero, T.G., Batten, M., Wheway, J., et al. (2002). Association of BAFF/BLyS overexpression and altered B cell differentiation with Sjögren's syndrome. J. Clin. Invest. 109, 59–68.

Haneji, N., Nakamura, T., Takio, K., Yanagi, K., Higashiyama, H., Saito, I., Noji, S., Sugino, H., and Hayashi, Y. (1997). Identification of α-fodrin as a candidate autoantigen in primary Sjögren's syndrome. Science 276, 604–607.

Hetz, C. (2012). The unfolded protein response: controlling cell fate decisions under ER stress and beyond. Nat. Rev. Mol. Cell Biol. 13, 89–102.

Higuchi, A., Shimmura, S., Takeuchi, T., Suematsu, M., and Tsubota, K. (2006). Elucidation of apoptosis induced by serum deprivation in cultured conjunctival epithelial cells. Br. J. Ophthalmol. 90, 760–764.

Hijioka, K., Matsuo, S., Eto-Kimura, A., Takeshige, K., and Muta, T. (2007). Induction of the nuclear IkappaB protein IkappaB-ζ upon stimulation of B cell antigen receptor. Biochem. Biophys. Res. Commun. 356, 476–480.

Hobeika, E., Thiemann, S., Storch, B., Jumaa, H., Nielsen, P.J., Pelanda, R., and Reth, M. (2006). Testing gene function early in the B cell lineage in mb1-cre mice. Proc. Natl. Acad. Sci. USA 103, 13789–13794.

Huang, M., Ida, H., Kamachi, M., Iwanaga, N., Izumi, Y., Tanaka, F., Aratake, K., Arima, K., Tamai, M., Hida, A., et al. (2005). Detection of apoptosis-specific autoantibodies directed against granzyme B-induced cleavage fragments of the SS-B (La) autoantigen in sera from patients with primary Sjögren's syndrome. Clin. Exp. Immunol. 142, 148–154.

Ishimaru, N., Saegusa, K., Yanagi, K., Haneji, N., Saito, I., and Hayashi, Y. (1999). Estrogen deficiency accelerates autoimmune exocrinopathy in murine Sjögren's syndrome through fas-mediated apoptosis. Am. J. Pathol. 155, 173–181.

Ito, M.R., Terasaki, S., Itoh, J., Katoh, H., Yonehara, S., and Nose, M. (1997). Rheumatic diseases in an MRL strain of mice with a deficit in the functional Fas ligand. Arthritis Rheum. 40, 1054–1063.

Kanki, H., Suzuki, H., and Itohara, S. (2006). High-efficiency CAG-FLPe deleter mice in C57BL/6J background. Exp. Anim. 55, 137–141.

Kitamura, T., Koshino, Y., Shibata, F., Oki, T., Nakajima, H., Nosaka, T., and Kumagai, H. (2003). Retrovirus-mediated gene transfer and expression cloning: powerful tools in functional genomics. Exp. Hematol. 31, 1007–1014.

Kong, L., Ogawa, N., Nakabayashi, T., Liu, G.T., D'Souza, E., McGuff, H.S., Guerrero, D., Talal, N., and Dang, H. (1997). Fas and Fas ligand expression in the salivary glands of patients with primary Sjögren's syndrome. Arthritis Rheum. 40, 87–97.

Li, H., Dai, M., and Zhuang, Y. (2004). A T cell intrinsic role of Id3 in a mouse model for primary Sjogren's syndrome. Immunity 21, 551–560.

Manganelli, P., and Fietta, P. (2003). Apoptosis and Sjögren syndrome. Semin. Arthritis Rheum. 33, 49–65.

Manoussakis, M.N., Dimitriou, I.D., Kapsogeorgou, E.K., Xanthou, G., Paikos, S., Polihronis, M., and Moutsopoulos, H.M. (1999). Expression of B7 costimulatory molecules by salivary gland epithelial cells in patients with Sjögren's syndrome. Arthritis Rheum. 42, 229–239.

Matsumura, R., Umemiya, K., Kagami, M., Tomioka, H., Tanabe, E., Sugiyama, T., Sueishi, M., Nakajima, A., Azuma, M., Okumura, K., and Sumida, T. (1998). Glandular and extraglandular expression of the Fas-Fas ligand and apoptosis in patients with Sjögren's syndrome. Clin. Exp. Rheumatol. 16, 561–568.

Mavragani, C.P., Tzioufas, A.G., and Moutsopoulos, H.M. (2000). Sjögren's syndrome: autoantibodies to cellular antigens. Clinical and molecular aspects. Int. Arch. Allergy Immunol. 123, 46–57.

Mitsias, D.I., Kapsogeorgou, E.K., and Moutsopoulos, H.M. (2006). Sjögren's syndrome: why autoimmune epithelitis? Oral Dis. 12, 523–532.

Morita, S., Kojima, T., and Kitamura, T. (2000). Plat-E: an efficient and stable system for transient packaging of retroviruses. Gene Ther. 7, 1063–1066.

Motoyama, M., Yamazaki, S., Eto-Kimura, A., Takeshige, K., and Muta, T. (2005). Positive and negative regulation of nuclear factor-kappaB-mediated transcription by IkappaB-ζ, an inducible nuclear protein. J. Biol. Chem. 280, 7444–7451.

Moutsopoulos, H.M., Hooks, J.J., Chan, C.C., Dalavanga, Y.A., Skopouli, F.N., and Detrick, B. (1986). HLA-DR expression by labial minor salivary gland tissues in Sjögren's syndrome. Ann. Rheum. Dis. 45, 677–683.

Nagaraju, K., Cox, A., Casciola-Rosen, L., and Rosen, A. (2001). Novel fragments of the Sjögren's syndrome autoantigens α-fodrin and type 3 muscarinic

acetylcholine receptor generated during cytotoxic lymphocyte granule-induced cell death. Arthritis Rheum. 44, 2376–2386.

Nakamura, H., Koji, T., Tominaga, M., Kawakami, A., Migita, K., Kawabe, Y., Nakamura, T., Shirabe, S., and Eguchi, K. (1998). Apoptosis in labial salivary glands from Sjögren's syndrome (SS) patients: comparison with human T lymphotropic virus-I (HTLV-I)-seronegative and -seropositive SS patients. Clin. Exp. Immunol. 114, 106–112.

Nenci, A., Huth, M., Funteh, A., Schmidt-Supprian, M., Bloch, W., Metzger, D., Chambon, P., Rajewsky, K., Krieg, T., Haase, I., and Pasparakis, M. (2006). Skin lesion development in a mouse model of incontinentia pigmenti is triggered by NEMO deficiency in epidermal keratinocytes and requires TNF signaling. Hum. Mol. Genet. 15, 531–542.

Okamoto, K., Iwai, Y., Oh-Hora, M., Yamamoto, M., Morio, T., Aoki, K., Ohya, K., Jetten, A.M., Akira, S., Muta, T., and Takayanagi, H. (2010). IkappaBzeta regulates T(H)17 development by cooperating with ROR nuclear receptors. Nature 464, 1381–1385.

Omori, E., Matsumoto, K., Sanjo, H., Sato, S., Akira, S., Smart, R.C., and Ninomiya-Tsuji, J. (2006). TAK1 is a master regulator of epidermal homeostasis involving skin inflammation and apoptosis. J. Biol. Chem. 281, 19610–19617.

Pasparakis, M., Courtois, G., Hafner, M., Schmidt-Supprian, M., Nenci, A., Toksoy, A., Krampert, M., Goebeler, M., Gillitzer, R., Israel, A., et al. (2002). TNF-mediated inflammatory skin disease in mice with epidermis-specific deletion of IKK2. Nature 417, 861–866.

Peng, B., Ling, J., Lee, A.J., Wang, Z., Chang, Z., Jin, W., Kang, Y., Zhang, R., Shim, D., Wang, H., et al. (2010). Defective feedback regulation of NF-kappaB underlies Sjogren's syndrome in mice with mutated kappaB enhancers of the IkappaBalpha promoter. Proc. Natl. Acad. Sci. USA 107, 15193–15198.

Pflugfelder, S.C., Jones, D., Ji, Z., Afonso, A., and Monroy, D. (1999). Altered cytokine balance in the tear fluid and conjunctiva of patients with Sjögren's syndrome keratoconjunctivitis sicca. Curr. Eye Res. 19, 201–211.

Polihronis, M., Tapinos, N.I., Theocharis, S.E., Economou, A., Kittas, C., and Moutsopoulos, H.M. (1998). Modes of epithelial cell death and repair in Sjögren's syndrome (SS). Clin. Exp. Immunol. 114, 485–490.

Rebholz, B., Haase, I., Eckelt, B., Paxian, S., Flaig, M.J., Ghoreschi, K., Nedospasov, S.A., Mailhammer, R., Debey-Pascher, S., Schultze, J.L., et al. (2007). Crosstalk between keratinocytes and adaptive immune cells in an IkappaBalpha protein-mediated inflammatory disease of the skin. Immunity 27, 296–307.

Saegusa, K., Ishimaru, N., Yanagi, K., Mishima, K., Arakaki, R., Suda, T., Saito, I., and Hayashi, Y. (2002). Prevention and induction of autoimmune exocrinopathy is dependent on pathogenic autoantigen cleavage in murine Sjögren's syndrome. J. Immunol. 169, 1050–1057.

Sakai, K., and Miyazaki, Ji. (1997). A transgenic mouse line that retains Cre recombinase activity in mature oocytes irrespective of the cre transgene transmission. Biochem. Biophys. Res. Commun. 237, 318–324.

Sano, S., Itami, S., Takeda, K., Tarutani, M., Yamaguchi, Y., Miura, H., Yoshikawa, K., Akira, S., and Takeda, J. (1999). Keratinocyte-specific ablation of Stat3 exhibits impaired skin remodeling, but does not affect skin morphogenesis. EMBO J. 18, 4657–4668.

Shiina, T., Konno, A., Oonuma, T., Kitamura, H., Imaoka, K., Takeda, N., Todokoro, K., and Morimatsu, M. (2004). Targeted disruption of MAIL, a nuclear IkappaB protein, leads to severe atopic dermatitis-like disease. J. Biol. Chem. 279, 55493–55498.

Shinkai, Y., Rathbun, G., Lam, K.P., Oltz, E.M., Stewart, V., Mendelsohn, M., Charron, J., Datta, M., Young, F., Stall, A.M., et al. (1992). RAG-2-deficient mice lack mature lymphocytes owing to inability to initiate V(D)J rearrangement. Cell 68, 855–867.

Takahama, Y., Ohishi, K., Tokoro, Y., Sugawara, T., Yoshimura, Y., Okabe, M., Kinoshita, T., and Takeda, J. (1998). Functional competence of T cells in the absence of glycosylphosphatidylinositol-anchored proteins caused by T cell-specific disruption of the Pig-a gene. Eur. J. Immunol. 28, 2159–2166.

Takeda, K., Noguchi, K., Shi, W., Tanaka, T., Matsumoto, M., Yoshida, N., Kishimoto, T., and Akira, S. (1997). Targeted disruption of the mouse Stat3

gene leads to early embryonic lethality. Proc. Natl. Acad. Sci. USA 94, 3801–3804.

Takeda, K., Kaisho, T., Yoshida, N., Takeda, J., Kishimoto, T., and Akira, S. (1998). Stat3 activation is responsible for IL-6-dependent T cell proliferation through preventing apoptosis: generation and characterization of T cell-specific Stat3-deficient mice. J. Immunol. 161, 4652–4660.

Taniguchi, T., Takata, M., Ikeda, A., Momotani, E., and Sekikawa, K. (1997). Failure of germinal center formation and impairment of response to endotoxin in tumor necrosis factor alpha-deficient mice. Lab. Invest. 77, 647–658.

Tarutani, M., Itami, S., Okabe, M., Ikawa, M., Tezuka, T., Yoshikawa, K., Kinoshita, T., and Takeda, J. (1997). Tissue-specific knockout of the mouse Pig-a gene reveals important roles for GPI-anchored proteins in skin development. Proc. Natl. Acad. Sci. USA 94, 7400–7405.

Ueta, M., Hamuro, J., Yamamoto, M., Kaseda, K., Akira, S., and Kinoshita, S. (2005). Spontaneous ocular surface inflammation and goblet cell disappearance in IκBζ gene-disrupted mice. Invest. Ophthalmol. Vis. Sci. 46, 579–588.

Ueta, M., Hamuro, J., Ueda, E., Katoh, N., Yamamoto, M., Takeda, K., Akira, S., and Kinoshita, S. (2008). Stat6-independent tissue inflammation occurs selectively on the ocular surface and perioral skin of IkappaBzeta-/- mice. Invest. Ophthalmol. Vis. Sci. 49, 3387–3394.

Vissink, A., Kalk, W.W., Mansour, K., Spijkervet, F.K., Bootsma, H., Roodenburg, J.L., Kallenberg, C.G., and Nieuw Amerongen, A.V. (2003). Comparison of lacrimal and salivary gland involvement in Sjögren's syndrome. Arch. Otolaryngol. Head Neck Surg. 129, 966–971.

Vitali, C., Bombardieri, S., Jonsson, R., Moutsopoulos, H.M., Alexander, E.L., Carsons, S.E., Daniels, T.E., Fox, P.C., Fox, R.I., Kassan, S.S., et al.; European Study Group on Classification Criteria for Sjögren's Syndrome. (2002). Classification criteria for Sjögren's syndrome: a revised version of the European criteria proposed by the American-European Consensus Group. Ann. Rheum. Dis. 61, 554–558.

Watanabe, S., Takeshige, K., and Muta, T. (2007). A cis-element in the 3′-untranslated region of IkappaB-ζ mRNA governs its stimulus-specific expression. Biochem. Biophys. Res. Commun. 356, 785–791.

Wu, A.J., Chen, Z.J., Tsokos, M., O'Connell, B.C., Ambudkar, I.S., and Baum, B.J. (1996). Interferon-γ induced cell death in a cultured human salivary gland cell line. J. Cell. Physiol. 167, 297–304.

Xiao, X., He, H., Lin, Z., Luo, P., He, H., Zhou, T., Zhou, Y., and Liu, Z. (2012). Therapeutic effects of epidermal growth factor on benzalkonium chloride-induced dry eye in a mouse model. Invest. Ophthalmol. Vis. Sci. 53, 191–197.

Yamamoto, M., Yamazaki, S., Uematsu, S., Sato, S., Hemmi, H., Hoshino, K., Kaisho, T., Kuwata, H., Takeuchi, O., Takeshige, K., et al. (2004). Regulation of Toll/IL-1-receptor-mediated gene expression by the inducible nuclear protein IkappaBzeta. Nature 430, 218–222.

Yamazaki, S., Muta, T., and Takeshige, K. (2001). A novel IkappaB protein, IkappaB-ζ, induced by proinflammatory stimuli, negatively regulates nuclear factor-kappaB in the nuclei. J. Biol. Chem. 276, 27657–27662.

Yamazaki, S., Muta, T., Matsuo, S., and Takeshige, K. (2005). Stimulus-specific induction of a novel nuclear factor-kappaB regulator, IkappaB-ζ, via Toll/Interleukin-1 receptor is mediated by mRNA stabilization. J. Biol. Chem. 280, 1678–1687.

Pillar-shaped stimulus electrode array for high-efficiency stimulation of fully implantable epiretinal prosthesis

Kang-Wook Lee[1], Yoshinobu Watanabe[2], Chikashi Kigure[2], Takafumi Fukushima[1], Mitsumasa Koyanagi[1] and Tetsu Tanaka[2]

[1] New Industry Creation Hatchery Center (NICHe), Tohoku University, 6-6-01 Aza-Aoba, Aramaki, Aoba-ku, Sendai 980-8579, Japan
[2] Department of Biomedical Engineering, Tohoku University, 6-6-01 Aza-Aoba, Aramaki, Aoba-ku, Sendai 980-8579, Japan

E-mail: link@lbc.mech.tohoku.ac.jp

Abstract
We developed a pillar-shaped microelectrode array (MEA) with varying heights for enhancing the spherical conformity of fully implantable epiretinal prosthesis comprising a 3D stacked retinal chip. The fabricated MEA is composed of 100 pillar electrodes with heights ranging from 60 to 80 μm. The Pt-coated Cu pillar electrode with a surface diameter of 70 μm and a height of 75 μm and the Pt planar electrode with a surface diameter of 70 μm have 24.6 and 125 kΩ impedances, respectively, at 1 kHz *in vitro* experiment. The pillar electrode shows lower impedance than the planar electrode because of a larger surface area. However, to avoid cross-talking between pillar electrodes, we developed a sidewall passivation process of the pillar electrode by using the surface tension of polyimide. The impedance of the isolated pillar electrode 116 kΩ at 1 kHz is similar to the impedance of the planar electrode, because they have similar electrode surface areas. The pillar-shaped MEA shows a better spherical conformity.

(Some figures may appear in colour only in the online journal)

1. Introduction

To date, a number of patients suffer from retinal diseases, such as retinitis pigmentosa (RP) and age-related macular degeneration (AMD). However, effective medical treatments for RP and AMD have yet to be established. In addition, it also is observed that the number of blind patients increases rapidly with the aging of society. Therefore, the alternative treatments for these diseases are strongly required. Photoreceptor cells in a retina play an important function in retinal cells by converting the visual information to neural signal.

However, in most cases, RP and AMD result from impairment of the photoreceptor cells that convert light signal to electrical signal in a retina. On the other hand, the other retinal cells, such as bipolar cells, horizontal cells and ganglion cells, remain normal [1, 2]. Accordingly, it will be possible to recover the patient's vision by stimulating the remaining retinal cells. A number of research groups have reported that light perception can be elicited by the electrical stimulation of the remaining retinal cells [3–6]. Recently, many studies have been reported for retinal prostheses in blind patients to restore visual sensation by electrical stimulation using stimulus electrodes [7–21]. Generally, retinal prosthesis has three indispensable components, such as a photodetector, a signal processing circuit and a stimulus current generator with a stimulus electrode array. The photodetector receives an optical signal from the outside and converts it to an electrical signal after which the processing circuits perform image processing, such as edge extraction and motion detection. Then, the stimulus current generator, placed on the surface of the retina, generates appropriate patterns of electrical current. Finally, the stimulus electrode array stimulates the remaining retinal cells. When the remaining retinal cells are activated by the stimulus current, blind patients would perceive a dot
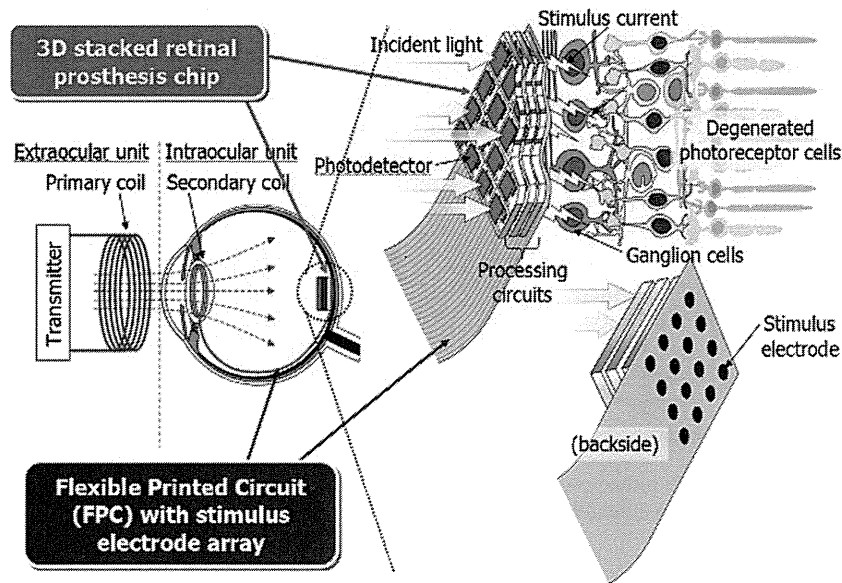
Figure 1. Configuration of fully implantable retinal prosthesis system comprising 3D stacked retinal chip, stimulus current generator with stimulus electrode array and coupling coils.

of light at each stimulation point. In conventional retinal prosthesis, only the stimulus current generator with a few tens of stimulus electrodes is implanted in the eyeball because of a small retinal area of approximately 3 mm^2, which is suitable for retinal chip implantation. Meanwhile, other devices, such as photodetector and processing circuits, are placed outside the eyeball. Therefore, the conventional retinal prosthesis is a large, heavy and complicated system. Moreover, the patients cannot use saccadic effect based on a high-speed eye movement. These disadvantages induce a low quality-of-life (QOL) to the patient. To resolve these issues and to implement similar performance with the human eye, a high-speed, high-performance and small-size artificial retina with saccadic function is required.

To realize such an artificial retina, we have proposed a fully implantable retinal prosthesis system comprising three-dimensional (3D) stacked retinal chip for transforming optical signal to electrical signal and generating stimulus current, microelectrode stimulus array for stimulating retina cells and coupling coils for power transmission as shown in figure 1. This retinal prosthesis can be fully implanted on the surface of the retina, unlike the other group's retinal prosthesis [22]. For realizing a fully implantable retinal prosthesis, we have developed some key components such as a stimulus current generator with a stimulus electrode array and a retinal prosthesis module [22–27].

Figure 2 shows a conceptual cross-sectional structure of 3D stacked retinal chip and stimulus microelectrode array (MEA). The 3D stacked retinal chip comprising photodetectors converts the optical signal received from outside the eyes into an electrical signal, the signal-processing circuits perform image processing, and the stimulus current generator generates appropriate electrical current pattern, bonded on a thin flexible cable with stimulus MEA to stimulate the remaining retinal cells. All component chips are vertically
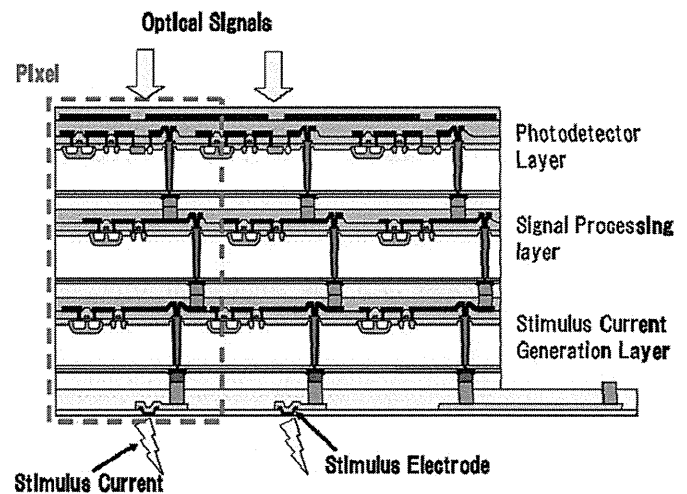

Figure 2. Cross-sectional structure of 3D stacked retinal chip and MEA.

stacked onto one die and electrically connected using high-density, short-length through-silicon vias (TSVs). This leads to a small-sized, light-weight, high fill-factor and high-resolution prosthesis retinal chip. By implanting the 3D stacked retinal chip into an eyeball, patients can employ their own lens and cornea and can rapidly shift a gaze point by moving the eyeball, leading to high-speed visual information processing such as a saccade effect. As the 3D stacked retinal chip has a layered structure similar to the human retina, photodetectors with more than 1000 pixels can be formed in the retinal chip.

To achieve highly efficient stimulation to the retina, it is necessary to establish uniform contact between the retinal cells and the stimulus microelectrodes. However, considering the curvature of the human eyeball, it is hard to make certain contacts to the retinal cells by a planar MEA owing to the distance between them, which is induced by the 3D stacked
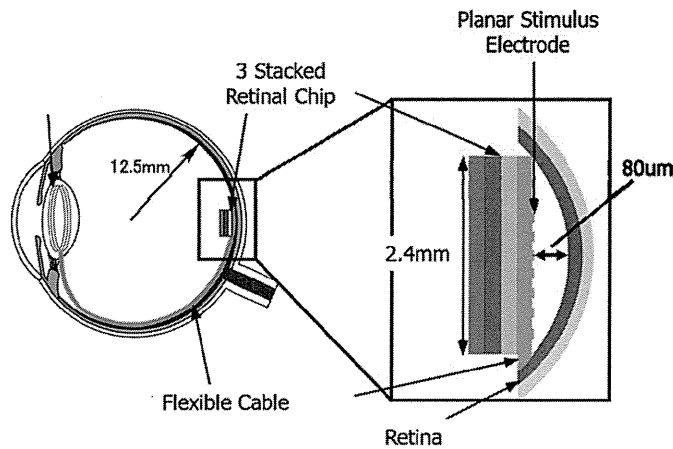
2

Figure 3. Configuration of fully implantable retinal prosthesis, in which 3D stacked retinal chip was bonded on a flexible cable with the planar-shaped stimulus MEA.

Figure 4. Conceptual relationship of the distance between planar stimulus electrodes and retinal cells in human eye.

retinal chip bonded to a flexible cable with the MEA, as shown in figure 3. We calculated the distance changes with the position from the center to the edge of the planar-shaped stimulus electrodes according to the curvature of the human eyeball by considering that the curvature radius of the human eyeball is 12.5 mm and the area of a 3D stacked artificial retina chip is 2.4 mm^2. There is a maximum distance of 82 μm at the center of the retinal prosthesis chip to the retinal cell in a curved focal plane as shown in figure 4. To achieve a high-resolution retinal prosthesis, it is necessary to stimulate only a target retinal cell. However, this long distance between the planar-shaped stimulus electrodes and the curved focal plane of the human eyeball may induce the low resolution because of a poor stimulation to the retinal cells, because the stimulus current from one stimulus electrode is widespread and stimulates unwanted neighboring retinal cells. This unwanted stimulation may induce tissue damage in neighboring retinal cells. Moreover, the relative distance from its target cell require rise in threshold, and more current will be theoretically necessary for efficient stimulation [28, 29]. It may induce a potential risk to damage the tissue, if the stimulation current level exceeds the level above the non-reversible reactions. To address this problem, penetrating electrodes, which can provide highly specific activation of the targeted neurons [29], have been developed for retinal prosthesis. However, these electrodes, mostly based on the Si technology, have been confirmed to incur acute and chronic damage, and even to lead to degeneration of both the interfaced tissue and the implanted device [30]. Hungar *et al* [31], Wang *et al* [32] and Koo *et al* [33] developed 3D-type flexible MEAs based on parylene and polyimide using Si mold technology for enhancing the spherical conformity of the retinal prosthesis in an eyeball. However, these approaches still have limitations, such as process difficulties and different electrode shapes. In particular, the different arrowhead shapes of electrodes stimulate retina cells differently according to the positions in the array because of the impedance difference at each electrode.

To solve these problems and to achieve highly efficient stimulation to retina cells, we proposed a pillar-shaped
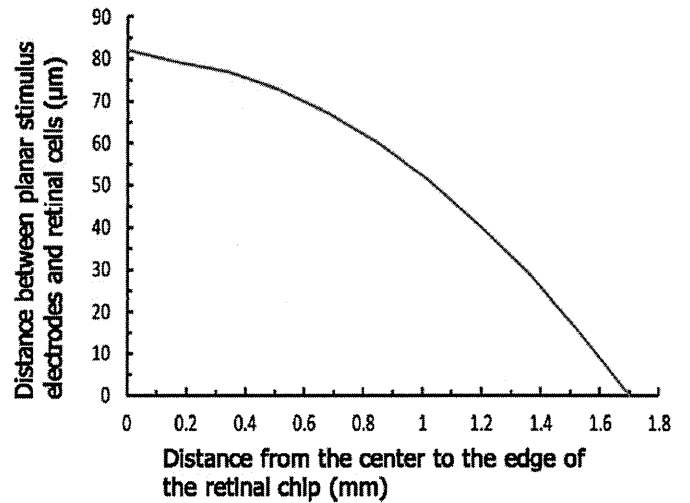
stimulus MEA with varying heights, but same surface areas according to the positions in the array using Si micromachining and peel-off processes. The height variation of electrodes allows each electrode to contact the spherical eyeball conformably and approach the stimulus target retinal cells closely. Moreover, the same surface area of electrodes allows stimulating target retinal cells at the same impedance. It can induce enhancement of the spherical conformity of fully implantable retinal prosthesis to the retinal cells in the human eyeball. However, by placing pillar electrodes that intentionally become a flatter surface of the retina chip across the curvature of the eyeball, it has a potential problem of defeating one of the key features of the normal eye, that of the curved focal plane, which does not have aberrations in the image because of differing distances from the lens. However, we assume that this is not as much of a problem, because the distance from the flat retina chip to the curved focal plane is around 80 μm, and it is too short compared with 20000 μm distance between the lens and the curved focal plane. Moreover, the depth of curvature of the human eyeball is slight, and the retina chip has a tiny area of 2.4 mm^2 and lesser thickness of 100 μm. Therefore, the entire retina chip can be in focus.

In this study, we fabricated the pillar-shaped stimulus MEA with varying heights, but the same surface areas, and characterized the impedance performance of the pillar electrode quantitatively compared with the planar electrode.

2. Design and fabrication of a pillar-shaped stimulus microelectrode

Figure 5 shows the configuration of fully implantable epiretinal prosthesis, in which a 3D stacked retinal chip was bonded to the flexible cable comprising pillar-shaped stimulus electrodes with varying heights. By these pillar electrodes, superior contact can be realized despite the various distances between the 3D stacked retinal chip and the target retinal cells in the spherical eyeball. Therefore, it can improve the stimulation
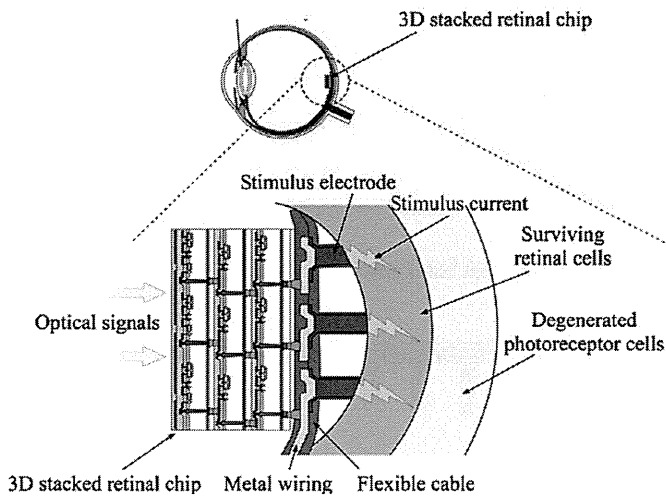
3

Figure 5. Configuration of fully implantable retinal prosthesis, in which 3D stacked retinal chip was bonded on a flexible cable with the pillar-shape stimulus MEA.
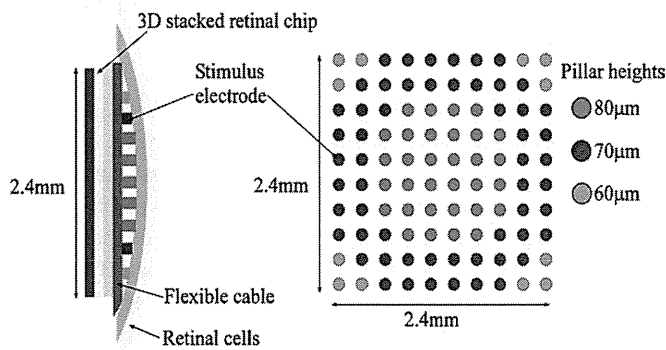

Figure 6. Layout of the pillar stimulus MEA consisting of 100 electrodes with varying heights.

efficiency to the retinal cells and induce highly qualitative resolution of the retinal prosthesis.

To evaluate the effectiveness of pillar electrodes, we proposed a pillar stimulus MEA composed of 100 electrodes, which have different heights of 60–80 μm in accordance with the pillar electrode position in the MEA, as shown in figure 6. The height variation of pillar electrodes allows each electrode to contact target retinal cells of the spherical eyeball conformably despite various distances between the retina chip and the retinal cells. This pillar MEA is formed in the polyimide-based flexible cable, the layout shown in figure 7. The flexible cable is divided into two parts of the retinal prosthesis module for implantation into an eyeball and the connection pad for a power supply. The flexible cable has a length of 35 mm and thickness of 25 μm. An array of 100 pillar stimulus electrodes is formed on the backside of the retinal prosthesis module part (front area) in the flexible cable. The retinal chip is mounted on the front side and electrically connected to stimulus electrodes through Cr/Au wires. The top surface diameter of stimulus pillar electrode is 70 μm, and the pitch between stimulus electrodes is 150 μm. Four holes, which were formed in the flexible cable, were used for
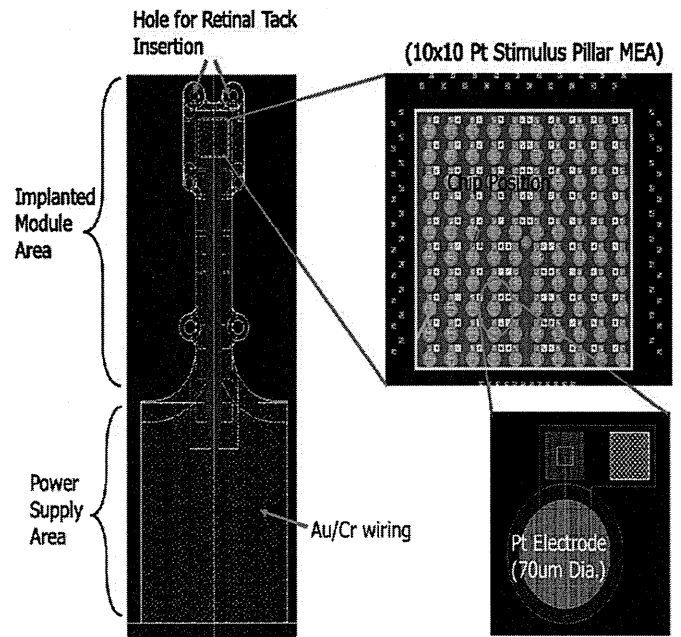

Figure 7. Layout of the flexible cable consisting of 100 Pr stimulus pillar electrodes.

fixation on the retina. Two holes in the edge area were inserted by retinal tacks inside the eyeball, and the other two holes in the middle area were sewn on the sclera outside the eyeball. Figure 8 shows the fabrication process flow of the flexible cable comprising the pillar stimulus MEA with varying heights. First, Si deep via holes with different depths were formed into a Si substrate by changing the cycling steps of plasma SF$_6$ etching and C$_4$F$_8$ passivation in the BOSCH process and using the multiple thickness of the SiO$_2$ layer. After removing the SiO$_2$ mask layer, sacrifice layers of sputtered-Al with 100 nm thickness and PECVD-SiO$_2$ with 200 nm thickness were deposited on the Si substrate and into the holes with the minimum sidewall step coverage of 40% and 60%, respectively. Positive-photosensitive polyimide (CRC 8600, T_g 300 °C) was spin coated on the Si substrate and patterned for the formation of a flexible cable consequently cured for 30 min at 350 °C. The polyimide layer was photo-lithographically patterned not to get down into the pillar holes. The resultant polyimide layer, which is used as a bottom layer of the flexible cable, has a thickness of around 3 μm. After photoresist (PR) patterning for the formation of stimulus electrodes, Pt layer of 100 nm thickness was deposited on the Si surface and into via holes with the minimum sidewall step coverage of 40%. Pt layer and PR layer were removed by a lift-off method using an ultrasonic method except for Pt layer on stimulus electrode areas. However, thin Pt layer of 40 nm thickness in the bottom area of the pillar electrode has the risk of deforming or fracturing during the contact with an eyeball. Therefore, it is necessary to enhance the strength of thin Pt pillar electrode. We proposed to fill Cu material into the pillar holes to improve the strength of the Pt pillar electrode. However, if Cu atoms diffuse to the eyeball passing through the Pt layer, it may induce contamination and consequently damage the retinal cells. To prevent the diffusion of Cu into the eyeball, a sputtered Ta layer of 500 nm thickness was deposed in the Pt pillar holes with
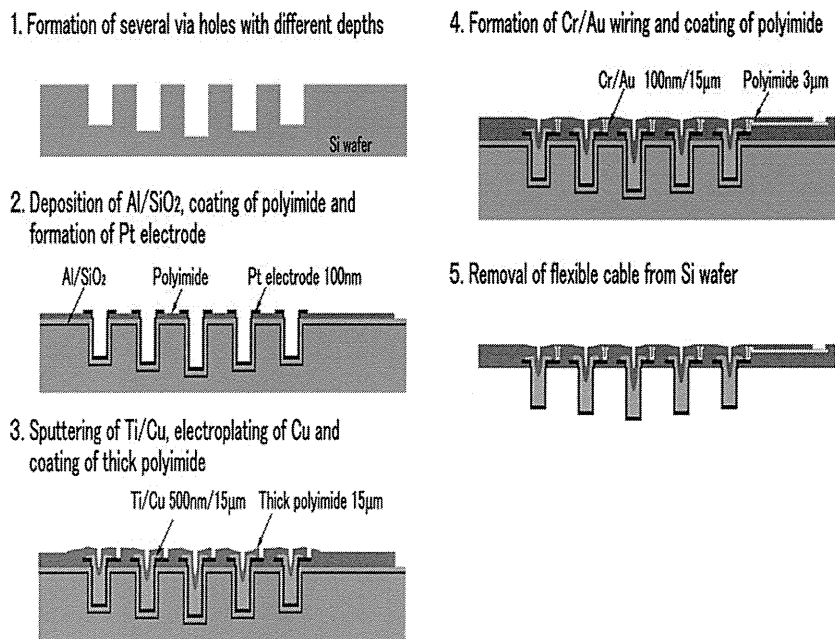
4

1. Formation of several via holes with different depths

2. Deposition of Al/SiO₂, coating of polyimide and formation of Pt electrode

3. Sputtering of Ti/Cu, electroplating of Cu and coating of thick polyimide

4. Formation of Cr/Au wiring and coating of polyimide

5. Removal of flexible cable from Si wafer

Figure 8. The fabrication process flow of the flexible cable comprising the pillar-shaped stimulus MEA with varying heights.

the minimum sidewall step coverage of 30%. The Ta layer is an attractive film as a Cu barrier because Ta has a high melting point that results in high activation energy for the diffusion process. Then, the Cu seed layer of 500 nm thickness was deposed in the pillar holes with the minimum sidewall step coverage of 40% by sputtering. After PR patterning, the Cu layer of 15 μm thickness was partially filled into the pillar holes using the electroplating process. Thick polyimide was spin coated, patterned and carefully cured for 30 min at 350 °C, with a resultant thickness of 15 μm. This polyimide layer may act as a main frame of the flexible cable and the barrier layer to Cu out-diffusion from the pillar electrode, because it covers the pillar electrodes. The Cr adhesion layer of 100 nm thickness and Au layer of 1 μm thickness were deposited sequentially by the sputtering process and patterned using the wet etching process to make metal wiring for power transmission. A thin polyimide layer (CRC 8600) was spin coated on metal wirings and patterned to open the pads only for power supply. The Au layer is exposed on the pad area and not the Cu layer, because Au may be biocompatible. Finally, the wafer was immersed into the buffered HF solution to etch sacrificial Al and SiO₂ layers and consequently peel-off the flexible cable with pillar-shaped stimulus electrodes from the Si substrate. The Au pad does not affect the HF solution during the peel-off process.

In our process, the formation of via holes with different depths by one-time Si etching process is the key. We utilized the difference of etching rate of Si and SiO₂ in the BOSCH etching process by using multiple thicknesses of SiO₂ hard mask. At first, a 70 nm thick SiO₂ layer was thermally oxidized on a Si substrate. By two-time local patterning and oxide dry etching, SiO₂ hard mask with different thicknesses of 0, 35 and 70 nm was formed on the Si substrate. Via holes with different depths of 60, 70 and 80 μm were fabricated concurrently by the

one-time Si BOSCH etching process using multiple thickness SiO₂ hard masks of 70, 35 and 0 nm, respectively, as shown in figure 9. Figure 10 shows the cross-sectional structure of the pillar electrode (*a*) and the photograph of the fabricated pillar electrode (*b*). For enhancing the strength of the Pt pillar electrode, a thick Cu layer of 15 μm thickness was filled well into the pillar holes using the electroplating process. Figure 11 shows the photograph of the fabricated flexible cable with the pillar MEA and the magnified picture of the pillar stimulus electrodes. As shown in the figure, the MEA consisting of 100 stimulus pillar electrodes with different heights ranging from 60 to 80 μm was successfully fabricated.

3. Evaluation of a pillar-shaped stimulus microelectrode

The impedance characteristics of the pillar stimulus electrode–electrolyte interface were evaluated using a Solartron1260 impedance/gain phase analyzer. Measurements were performed within a frequency range from 100 Hz to 100 kHz using 10 mV ac sine signals by immersing the pillar MEA into the 0.9% saline solution. An Ag/AgCl electrode and the pillar electrode were used as a reference electrode along with a counter electrode as shown in figure 12.

To evaluate the impedance characteristics of the pillar electrode, we compared them with the impedance characteristics of a Pt planar electrode with a surface diameter of 70 μm. Figure 13 shows the fabrication process (*a*) and the photograph (*b*) of the flexible cable with the Pt planar electrode array. Positive-photosensitive polyimide (CRC 8600) was spin coated on the Si substrate and patterned for the formation of a flexible cable consequently cured for 30 min at 350 °C. The resultant polyimide layer, which is used as a bottom layer of the flexible cable, has a thickness of around 5 μm. After
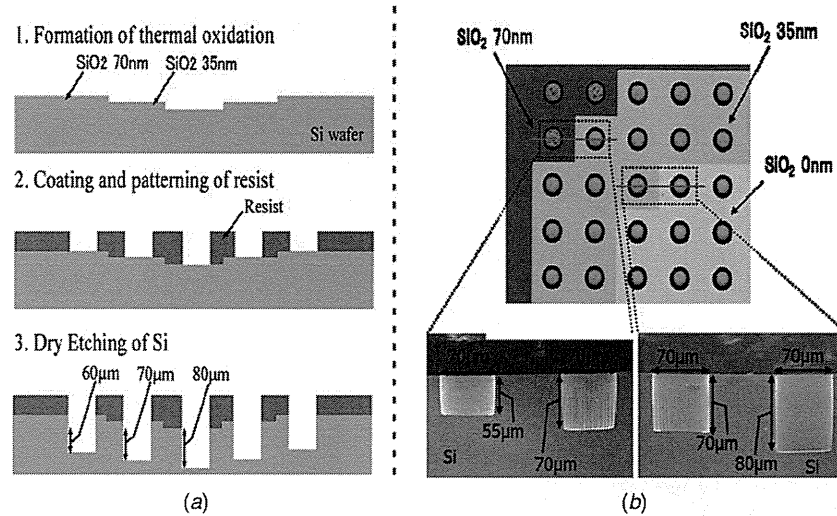
5

Figure 9. (*a*) The fabrication process flow and (*b*) the photograph of via holes with different heights.
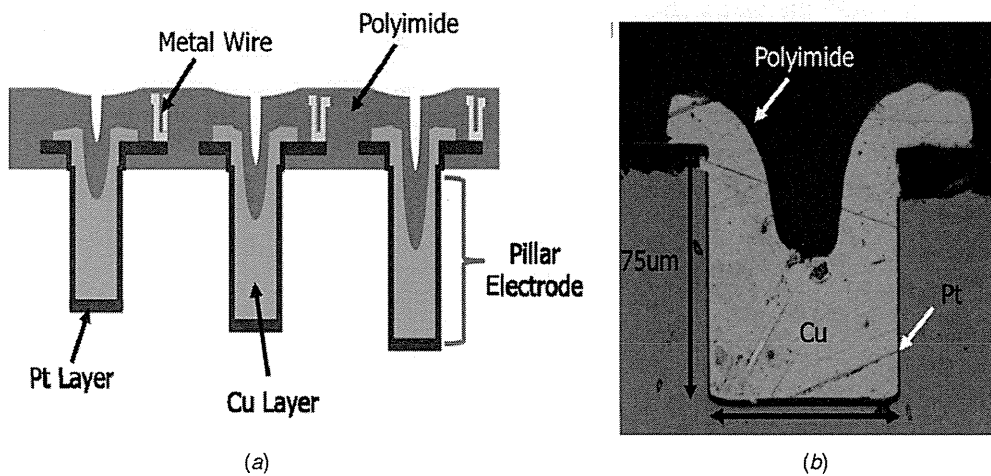

Figure 10. (*a*) Cross-sectional structure of pillar electrodes and (*b*) the photograph of the fabricated pillar electrode.

PR patterning for the formation of a stimulus electrode, the Pt layer of 100 nm thickness was deposited as a stimulus electrode material. The Cr adhesion layer of 100 nm thickness and Au wire of 1 μm thickness were patterned using the sputtering and wet etching processes for the power transmission. Thick polyimide was spin coated, patterned, and carefully cured for 30 min at 350 °C, where it has a resultant thickness of 15 μm. It acts as the main frame of the flexible cable.

Figure 14 shows the impedance characteristics of the pillar electrode and the planar electrode depending on frequencies. The impedances of the pillar and the planar electrodes are 24.6 and 125 kΩ at 1 kHz, respectively. The total surface areas of the pillar electrode (70 μm diameter, 75 μm height) and the planar electrode (70 μm diameter) are theoretically 20 332 and 3846 μm^2. The impedance decrement ratio (1/5.07) of the pillar electrode to the planar electrode is similar, with the difference ratio of the total surface area between them being 5.28. It indicates that the entire surface area of the pillar electrode functions as the stimulus electrode. A large surface area of the pillar electrode reduces the electrode impedance. Therefore, the pillar electrode with lower

impedance could contribute to reduce the amount of damage from the stimulation of the retinal cells because of lower charge density [29].

However, the pillar electrode has the risk that it stimulates only a target retinal cell, because of a cross-talking with neighboring electrodes and, consequently, unwanted stimulation around the retinal cells, because the entire surface of the pillar electrode would function as shown in figure 15. To solve this potential problem, we developed a sidewall passivation process of the pillar electrode by using the liquid surface tension as shown in figure 16. The resist block area was formed surrounding the pillar MEA area by PR patterning. The polyimide material (CRC 8600) of 3 μL controlled volume was poured carefully into the edge area of the photoresist mold. Then, the polyimide material was spread into the MEA area and coated on the sidewalls of the pillar electrodes by using liquid surface tension except for the top areas of the electrodes to contact the target retinal cells. If the volume is too large, it would coat the top of the pillars as well. To make the clear surface of the pillar electrode, a plasma-cleaning process known as descumming that use O_2 reactive ion etch,
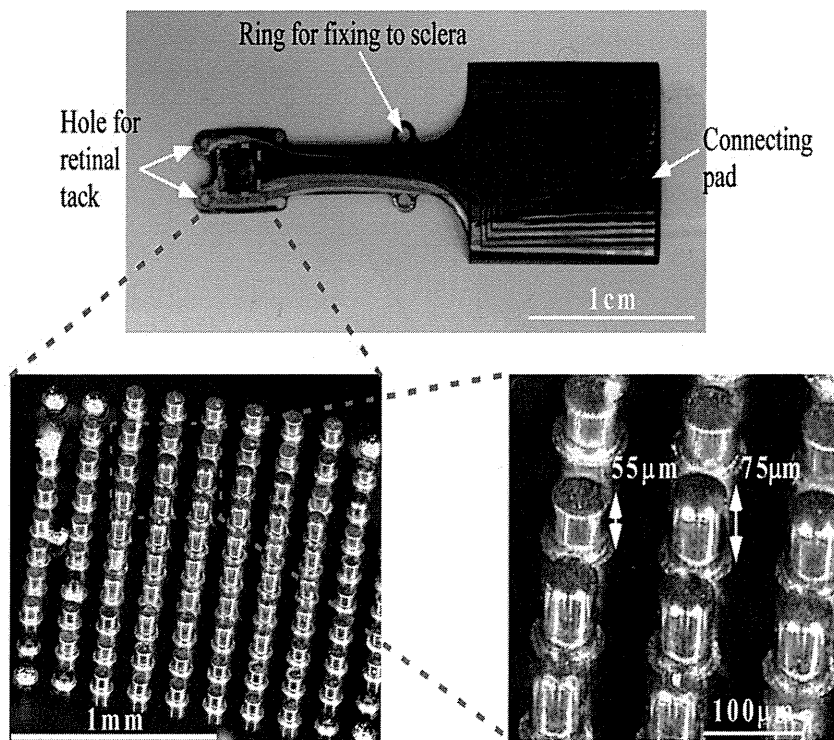
6

Figure 11. Photographs of the flexible cable comprising 100 stimulus pillar electrodes with different heights.
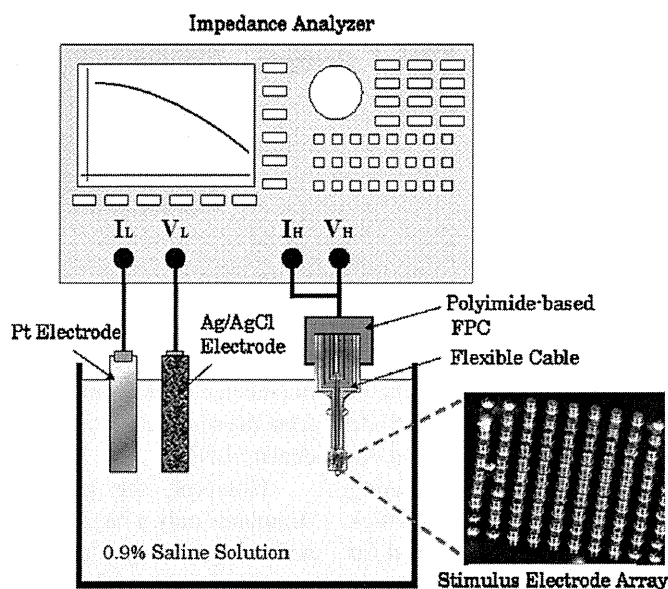

Figure 12. The setup for the three-point impedance measurement.

was lightly applied for 30 s. Figure 17 shows the photographs of the pillar electrode array in which the sidewalls of the pillar electrodes were successfully coated by the polyimide layer except that the top surface area was not coated. However, some sidewall areas near the top surface were not covered perfectly. Figure 18 shows the impedance characteristics of isolated and non-isolated pillar electrodes depending on the frequency. The impedance of the non-isolated pillar electrode is 24.6 kΩ, whereas the impedance of the isolated pillar electrode is 116 kΩ at 1 kHz, respectively. The impedance

of the isolated pillar electrode is similar to the impedance of the planar electrode of 125 kΩ at 1 kHz (as shown in figure 14). It indicates that the sidewall of the pillar electrode was isolated well by the polyimide layer; therefore, the top surface area of the pillar electrode functioned solely as the stimulus electrode. Ideally, the impedances of the isolated pillar electrode and the planar electrode should be the same. However, the impedance of the isolated pillar electrode is a little small, because some sidewall area near the top surface was not covered (as shown in figure 17). The increased surface
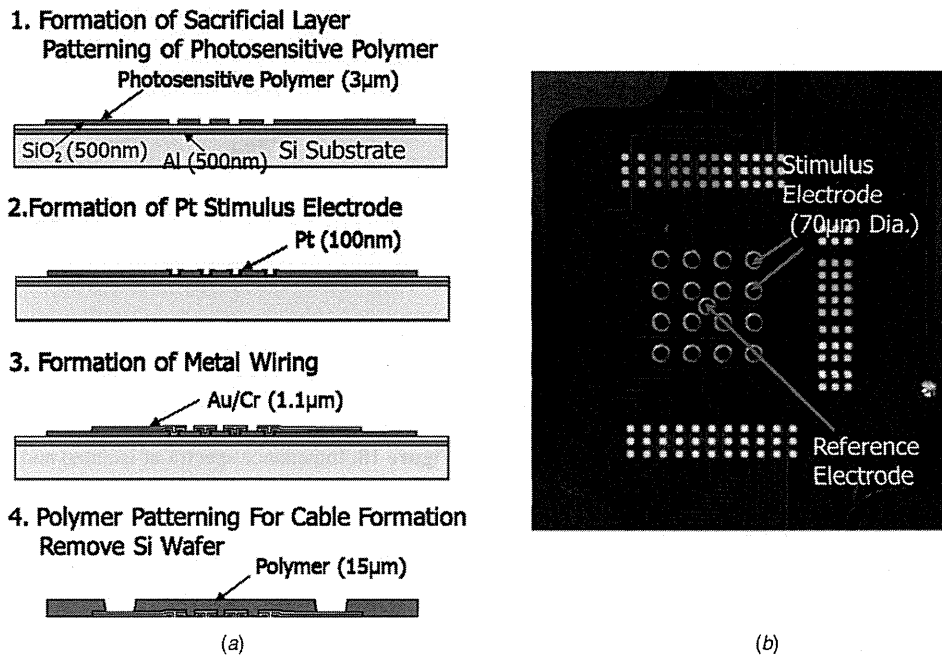
7

1. Formation of Sacrificial Layer
   Patterning of Photosensitive Polymer
   Photosensitive Polymer (3μm)

SiO₂ (500nm) Al (500nm) Si Substrate

2. Formation of Pt Stimulus Electrode
   Pt (100nm)

3. Formation of Metal Wiring
   Au/Cr (1.1μm)

4. Polymer Patterning For Cable Formation
   Remove Si Wafer
   Polymer (15μm)

(a)

Stimulus
Electrode
(70μm Dia.)

Reference
Electrode

(b)

Figure 13. (*a*) The fabrication process and (*b*) the photograph of the flexible cable with the Pt planar electrode array.
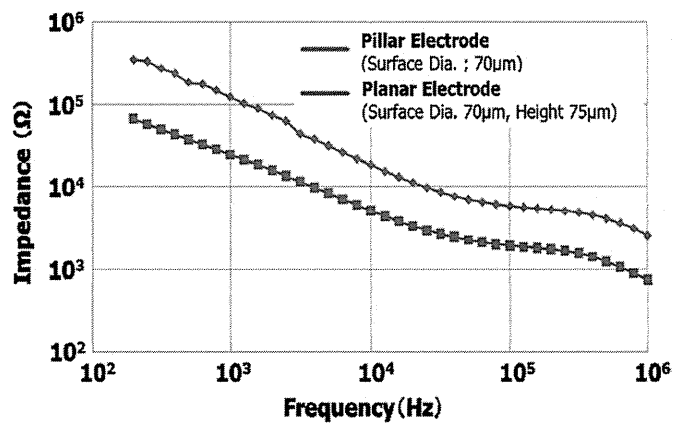
Figure 14. Impedance spectra of the planar electrode and the pillar electrode with 70 μm diameter size depending on frequencies.
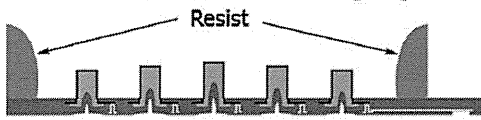

Flexible cable

Pillar stimulus electrode

Electrode cross-talk   Un-wanted stimulating

Surviving retinal cells   Degenerated photoreceptor cells
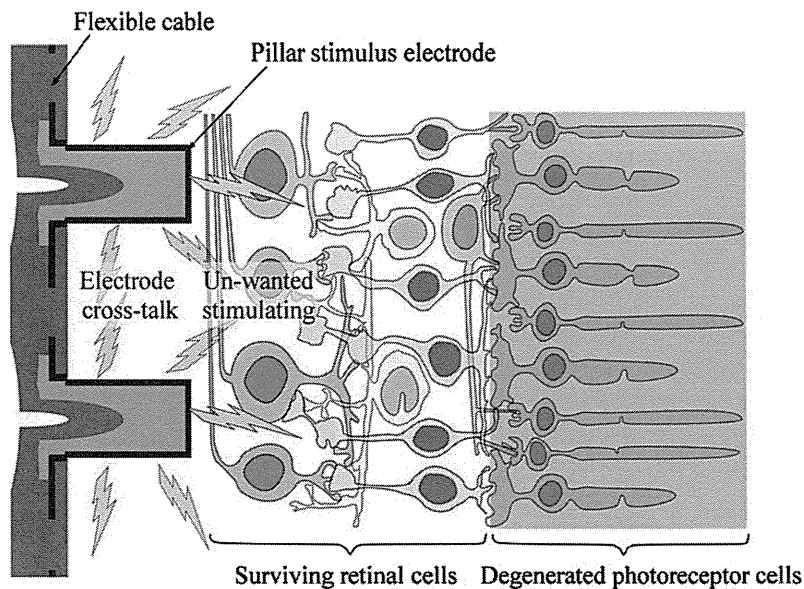
Figure 15. Concept of electrode cross-talk of a pillar stimulus electrode.

8

1. Flexible Cable with Pillar Electrodes

2. Formation of Resist Blocking Layer
Resist

3. Pouring & Curing of Polyimide
Polyimide
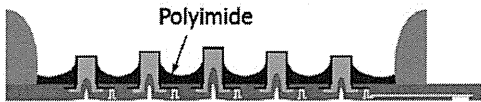
4. Passivation of Electrodes Sidewall by Polyimide

Figure 16. The sidewall isolation process flow of a pillar electrode.

area (4145 μm^2) induces decreased impedance than the planar electrode (3846 μm^2). However, this result shows a potential issue of differing impedances of the isolated pillar electrodes in the MEA. It is necessary to improve the sidewall passivation process.

To characterize the spherical conformity of the pillar electrode, the contacting behaviors of the pillar-shaped stimulus MEA and the planar stimulus MEA were evaluated. The fabricated MEA pricked an agar gel, which was cured into a spherical shape. A 2.5% agar has Young's modulus of 22 kPa [34], which is similar to Young's modulus of the retina (20 kPa) [35]. An agar gel (2.5%) was composed and then cured into an eyeball shape with a spherical mold [33]. The planar and the pillar stimulus MEAs were attached on the inside of the spherical-shaped agar, respectively. After detaching the curved MEAs, the agar surfaces were measured using an optical microscope as shown in figure 19. In the case of the planar MEA, any shape of the electrodes was not observed
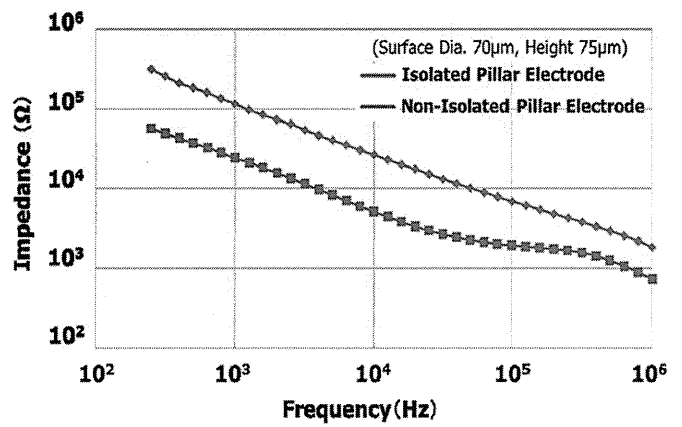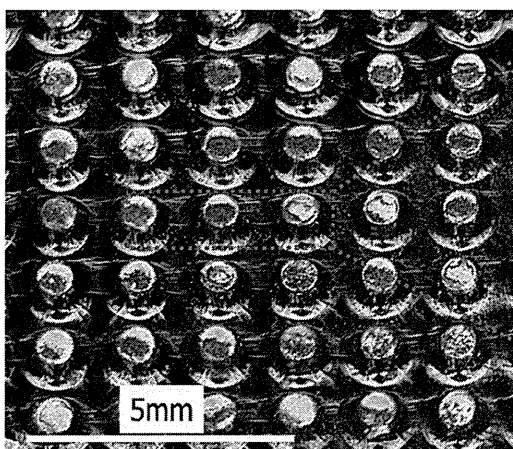
Figure 18. Impedance spectra of isolated and non-isolated pillar electrodes depending on frequencies.

from the agar surface as shown in 19(*a*). In the case of the pillar MEA, meanwhile, the extruded electrode array pattern was observed from the agar surface as shown in 19(*b*). However, the extruded array pattern is not clear and non-uniform. We assume that the pillar MEA was contacted manually to the agar surface, and therefore, it was not uniformly in contact with the agar surface. Even the electrode impression results are not clear sufficiently, we understand the difference of the conformity characteristics between the planar MEA and the pillar MEA. This shows the advantage achieved by highly efficient stimulation to the retina cells in the spherical eyeball.

In this study, we implemented the pillar-shaped stimulus MEA with varying heights to improve the stimulation efficiency to the retina cells and, consequently, induce highly qualitative resolution of the retinal prosthesis. However, this epiretinal approach, in which the device is implanted into the vitreous cavity and attached to the inner retinal surface, has relevant issues such as possible difficulties in chronic attachment of the 3D stacked retinal prosthesis to the retina. It requires optimization of the epiretinal design and improvement of surgical techniques for realizing the fully implantable epiretinal prosthesis.
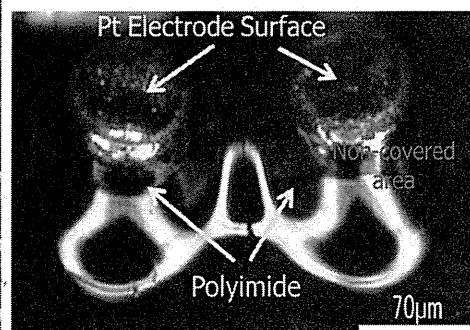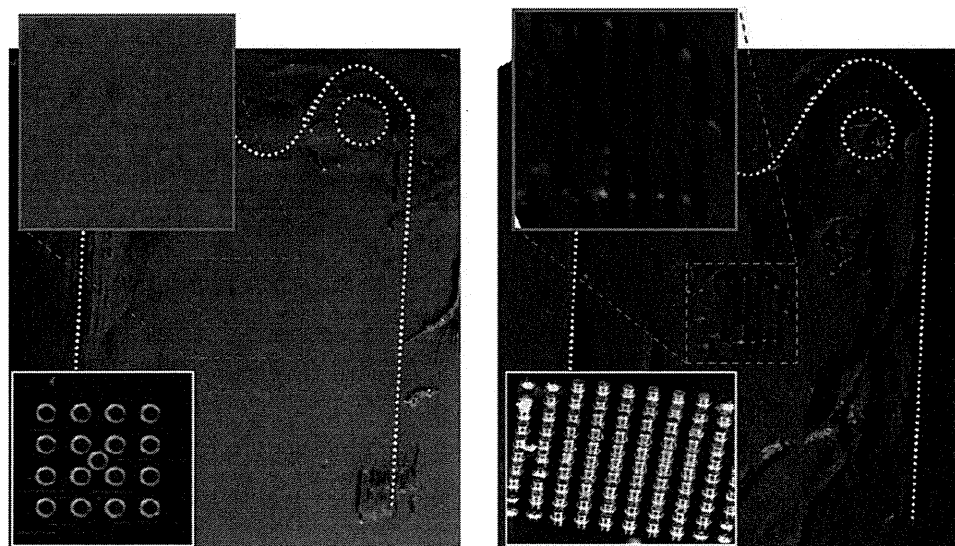
Figure 17. Photographs of the pillar electrode array partially coated by a biocompatible polyimide layer.

9

(a) **After attaching the planar-shape MEA**   (b) **After attaching the pillar-shape MEA**

Figure 19. The agar gel surfaces after attaching (*a*) the planar MEA and (*b*) the pillar MEA, respectively.

4. Conclusion

The pillar-shaped stimulus MEA with varying heights was fabricated for enhancing the spherical conformity of the fully implantable epiretinal prosthesis. The fabricated MEA is composed of 100 pillar electrodes with heights ranging from 60 to 80 μm. The Pt-coated Cu pillar electrode with a surface diameter of 70 μm and a height of 75 μm and the Pt planar electrode with a surface diameter of 70 μm have 24.6 and 125 kΩ impedances, respectively, at 1 kHz *in vitro* experiment. The pillar electrode shows lower impedance than the planar electrode because of a large electrode surface area. However, to avoid cross-talking between pillar electrodes, we developed a sidewall passivation process of the pillar electrode by using the surface tension of polyimide. The impedance of the isolated pillar electrode 116 kΩ at 1 kHz is similar to the impedance of the planar electrode, because they have similar electrode surface areas. The pillar-shaped MEA shows a better spherical conformity.

Acknowledgments

References

[1] Santos A, Humayun M S Jr, Greenburg R J, de Juan E, Marsh M J, Klock I B and Milam A H 1997 *Arch. Ophthalmol.* **115** 511–5
[2] Medeiros N E and Curcio C A 2001 *Invest. Ophthalmol. Vis. Sci.* **42** 795–803
[3] Humayun M S, Dagnelie G Jr, de Juan E, Greenberg R J, Propst R H and Phillips H 1996 *Arch. Ophthalmol.* **114** 40–6
[4] Chow A Y and Chow V Y 1997 *Neurosci. Lett.* **225** 13–6
[5] Eckmiller R 1997 *Ophthalmic Res.* **29** 281–9
[6] Zrenner E *et al* 1997 *Ophthalmic Res.* **29** 269–80
[7] Zrenner E 2002 *Science* **295** 1022–5
[8] Humayun M S, Propst R, de Juan E, McCormick K Jr and Hickingbotham D 1994 *Arch. Ophthalmol.* **112** 110–6
[9] Wyatt J and Rizzo 1996 *IEEE Spectr.* **33** 47–53
[10] Chow A Y and Peachey N S 1998 *Ophthalmic Res.* **30** 195–6
[11] Liu W, Vichienchom K, Clements M, DeMarco S C, Hughes C, McGucken E, Humayun M S, de Juan E, Weiland J D and Greenberg R 2000 *IEEE J. Solid-State Circuits* **35** 1487–97
[12] Margalit E *et al* 2003 *J. Neurosci. Methods* **123** 129–37
[13] Humayun M S, Juan E, Weiland J E, Dagnelie G, Katona S, Greenberg R and Suzuki S 1999 *Vis. Res.* **39** 2569–76
[14] Ohta J, Yoshida N, Kagawa K and Nunoshita M 2002 *Japan. J. Appl. Phys.* **41** 2322–5
[15] Scribner D *et al* 2007 *IEEE Trans. Biomed. Circuits Syst.* **1** 73–83
[16] Schanze T, Hesse L, Lau C, Greve N, Haberer W, Kammer S, Doerge T, Rentzos A and Stieglitz T 2007 *IEEE Trans. Biomed. Circuits Syst.* **54** 983–92
[17] Zrenner E 2002 *Ophthalmologica* **216** 8–20
[18] Kurino H, Lee K W, Nakamura T, Sakuma K, Park K T, Miyakawa N, Shimazutsu H, Kim K Y, Inamura K and Koyanagi M 1999 *Int. Electron Devices Meeting Technical Digest* pp 879–82
[19] Chow A Y, Chow V Y, Packo K H, Pollack J S, Peyman G A and Schuchard R 2004 *Arch. Ophthalmol.* **122** 460–9
[20] Chow A Y, Bittner A K and Pardue M T 2010 *Trans. Am. Ophthalmol. Soc.* **108** 120–54
[21] Zrenner E *et al* 2010 *Proc. R. Soc.* B **278** 1489–97
[22] Koyanagi M, Nakagawa Y, Lee K W, Nakamura T, Yamada Y, Inamura K, Park K T and Kurino H 2001 *Int. Solid-State Circuit Conf. Digest of Technical Papers* pp 270–1
[23] Deguchi J, Watanabe T, Motonami K, Sugimura T, Tomita H, Shim J C, Kurino H, Tamai M and Koyanagi M 2004 *Int. Conf. on Solid State Devices and Materials (Extended Abstracts)* pp 350–1

10

[24] Deguchi J, Watanabe T, Nakamura T, Nakagawa Y, Fukushima T, Shim J C, Kurino H, Abe T, Tamai M and Koyanagi M 2004 *Japan. J. Appl. Phys.* **43** 1685–9

[25] Motonami K, Watanabe T, Deguchi J, Fukushima T, Tomita H, Sugano E, Sato M, Kurino H, Tamai M and Koyanagi M 2006 *Japan. J. Appl. Phys.* **45** 3784–8

[26] Watanabe T, Kobayashi R, Komiya K, Fukushima T, Tomit H, Sugano E, Kurino H, Tanaka T, Tamai M and Koyanagi M 2007 *Japan. J. Appl. Phys.* **46** 2785–91

[27] Tanaka T, Sato K, Komiya K, Kobayashi T, Watanabe T, Fukushima T, Tomita H, Kurino H, Tamai M and Koyanagi M 2007 *Int. Electron. Devices Meeting Tech. Digest* pp 1016–9

[28] Ahuja A K, Behrend M R, Kuroda M, Humayun M S and Weiland J D 2008 *IEEE Trans. Biomed. Eng.* **55** 1744–53

[29] Margalit E *et al* 2002 Surv. Ophthalmol. **47** 335–6

[30] Humayun M S 2001 *Trans. Am. Ophthalmol. Soc.* **99** 271–300

[31] Hungar K, Gortz M, Slavcheva E, Spainer G, Weidig C and Mokwa W 2005 *Sensors Actuators* A 172–8

[32] Wang R, Huang X, Liu G, Wang W, Dong F and Li Z 2010 *J. Microelectromech. Syst.* **19** 367–74

[33] Koo K, Lee S, Bae S, Seo J, Chung H and Cho D 2011 *J. Microelectromech. Syst.* **20** 251–9

[34] Stolz M, Raiteri R, Daniels A U, VanLandingham M R, Baschong W and Aebi U 2004 *Biophys. J.* **86** 3269–83

[35] Jones I L, Warner M and Stevens J D 1992 *Eye* **6** 556–9

11
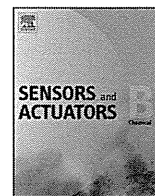
High-speed chemical imaging system based on front-side-illuminated LAPS

Akinori Itabashi[a], Naoki Kosaka[b], Ko-ichiro Miyamoto[a,*], Torsten Wagner[a], Michael J. Schöning[c,d], Tatsuo Yoshinobu[a,b]

[a] Department of Electronic Engineering, Tohoku University, 6-6-05 Aza-Aoba, Aramaki, Aoba-ku, Sendai 980-8579, Japan
[b] Department of Biomedical Engineering, Tohoku University, 6-6-05 Aza-Aoba, Aramaki, Aoba-ku, Sendai 980-8579, Japan
[c] Institute of Nano- and Biotechnologies, Aachen University of Applied Sciences, Heinrich-Mußmann Straße 1, 52428 Jülich, Germany
[d] Peter Grünberg Institute (PGI-8), Research Centre Jülich, 52425 Jülich, Germany

ARTICLE INFO

ABSTRACT

The chemical imaging sensor is a semiconductor-based chemical sensor that can visualize the spatial distribution of specific ions on the sensing surface. The conventional chemical imaging system based on the light-addressable potentiometric sensor (LAPS), however, required a long time to obtain a chemical image, due to the slow mechanical scan of a single light beam. For high-speed imaging, a plurality of light beams modulated at different frequencies can be employed to measure the ion concentrations simultaneously at different locations on the sensor plate by frequency division multiplex (FDM). However, the conventional measurement geometry of back-side illumination limited the bandwidth of the modulation frequency required for FDM measurement, because of the low-pass filtering characteristics of carrier diffusion in the Si substrate. In this study, a high-speed chemical imaging system based on front-side-illuminated LAPS was developed, which achieved high-speed spatiotemporal recording of pH change at a rate of 70 frames per second.

1. Introduction

The light-addressable potentiometric sensor (LAPS) [1] belongs to the family of semiconductor-based chemical sensors with an electrolyte–insulator–semiconductor (EIS) structure. The width of the depletion layer in the Si substrate responds to the ion concentration on the sensing surface, and the variation of its capacitance is read out in the form of AC photocurrent induced by illumination of the sensor plate with a modulated light. The most advantageous point of the LAPS measurement is that the measurement area can be defined by illumination. Based on this addressability of LAPS, we developed the chemical imaging sensor [2], which could visualize the two-dimensional distribution of specific ions in the solution on the sensing surface.

In a conventional chemical imaging system based on LAPS, a scanning light beam was used to obtain a two-dimensional map of the ion concentration. Due to the mechanical scan, however, a typical scan time to acquire a chemical image at a resolution of 128 × 128 pixels was about 3 min, which was too long to analyze the dynamics of chemical reactions.

Frequency division muliplex (FDM) [3] is one of the methods for high-speed chemical imaging, in which a plurality of light beams modulated at different frequencies are employed to read out the ion concentrations at different locations in parallel as shown in Fig. 1. In this case, the photocurrent signal is a superposition of all frequency components and each component can be individually extracted by Fourier analysis. Based on FDM-LAPS, we developed a chemical image scanner system [4], which employed a linear array of 16 LEDs to scan a chemical image at a resolution of 16 × 128 pixels. The scan time was reduced to 6.4 s, which, however, was still slow in comparison, for example, to the pH imaging sensor based on the charge coupled device (CCD) technology [5,6]. In our previous study, we developed a chemical movie recording system based on FDM and a two-dimensional array of LEDs. Using a two-dimensional array of LEDs as a light source, the slow mechanical scan of the conventional system was replaced by much faster electrical switching and a high-speed imaging at a frame rate of 10 fps (frames per second) was achieved [7].

In FDM, the required bandwidth of the modulation frequency is given by (number of light beams) × (frequency spacing) and the time window of Fourier analysis or the sampling time must be at least as long as 1/(frequency spacing). For high-speed chemical imaging, therefore, a wide bandwidth of frequency is required to increase the multiplicity and to reduce the time window. Here, two different geometries are possible in LAPS measurement [8] as shown in Fig. 2. Those are front-side and back-side illuminations,